

# Simulation environment for the C14 experiment

*Pro Gradu, 23.12.2016*

*Author:*

ROOPE SARALA

*Supervisors:*

TIMO ENQVIST, KAI LOO



JYVÄSKYLÄN YLIOPISTO  
FYSIKAN LAITOS

## TIIVISTELMÄ

Suuria tuikeaineilmaisimia käytetään erityisesti neutriinofysiikan kokeissa, joissa tutkitaan muun muassa aurinkoneutriinoja, neutriinotonta kaksinkertaista beetahajoamista sekä pimeää ainetta. Näissä kokeissa mitattava signaali on hyvin heikko, minkä vuoksi häiriöiden minimoiminen on hyvin tärkeää. Yksi suurimmista häiriötekijöistä on tuikeaineen sisältämä radiohiili, jonka taustasäteily käytännössä estää signaalin havaitsemisen noin 200 keV:iin saakka.

Radiohiili ( $^{14}\text{C}$ ) on hiilen luonnossa esiintyvä beeta-aktiivinen isotooppi, jonka puoliintumisaika on noin 5730 vuotta. Sitä syntyy pääasiassa kosmisen säteilyn osuessa yläilmakehän typpi-atomeihin, jonka seurauksena radiohiiltä on kaikessa orgaanisessa aineessa vähäisiä määriä. Tuoreessa aineessa radiohiilipitoisuus on noin  $10^{-12}$ . Suuren mittaluokan kokeissa käytetyt tuikeaineet ovat usein jalostettu raakaöljystä. Iän perusteella öljyn radiohiilipitoisuus olisi luokkaa  $10^{-21}$ , mutta todellisuudessa se on lähempänä arvoa  $10^{-17}$ , sillä öljyyn muodostuu lisää radiohiiltä sitä ympäröivän kiven säteilyn vaikutuksesta.

Radiohiilen aiheuttaman taustan vähentäminen hyödyttäisi siis kaikkia tulevia neutriinokokeita merkittävästi. Tätä tarkoitusta varten on rakennettu C14-konsentraatiomittauslaitteisto Pyhäsalmen kaivokselle CallioLab-tutkimuskeskukseen tutkimaan eri öljylähteistä valmistettuja tuikeaineita. Kokeen tavoitteena on löytää tuikeainenäyte, jonka radiohiilipitoisuus olisi mahdollisimman alhainen, mielellään alle  $10^{-18}$ . Laitteisto koostuu 1,6 litraisesta sylinterin muotoisesta tuikeainesäiliöstä, kahdesta lieriön muotoisesta valonjohtimesta ja kahdesta matalan aktiivisuuden valomonistinputkesta, minkä lisäksi laitteisto on kääritty heijastavaan folioon valontuoton parantamiseksi. Jotta ulkoisen taustasäteilyn vaikutus saataisiin minimoitua, laitteisto on ympäröity viiden senttimetrin kerroksilla lyijyä ja kuparia.

Tässä työssä on rakennettu simulaatioympäristö ymmärtämään paremmin C14-laitteiston toimintaa käyttäen C++ pohjaista Geant4-simulaatiotyökalua. Simulaatioympäristö soveltuu esimerkiksi mittaustalteen energioresoluution tutkimiseen, geometrian optimointiin, erilaisten sisäisten taustakomponenttien ja tuikeaineiden tutkimiseen. Tämän lisäksi tässä työssä on simulaatioympäristöä käyttäen tutkittu C14-laitteiston energiavastetta elektroneille ja alfahiukkasille sekä sisäisten komponenttien taustasignaalia verrattuna radiohiilen taustasignaaliin. Simulaatiotulokset osoittavat, että laitteiston valontuotto on paikkariippuvainen, mikäli heijastavaa foliota ei käytetä, ja myös riippuvainen folion todellisesta heijastavuudesta. Tämän seurauksena energioresoluutio on selvästi parempi kun folio on käytössä. Sisäisten taustakomponenttien vaikutus on vähäinen verrattuna radiohiilen signaaliin, ja selvästi suurin mittaussignaalia häiritsevä taustakomponentti on valomonistinputkista tuleva  $\gamma$ -säteily.

## ABSTRACT

In this thesis, a simulation environment utilizing Geant4 simulation toolkit was constructed to study the C14 experiment located at the Pyhäsalmi Mine, Finland. The C14 experiment aims to find a liquid scintillator sample with the least amount of  $^{14}\text{C}$ , the radioactive isotope of carbon, with concentration preferably less than  $10^{-18}$ . The scintillator detector used in the experiment consists of a 1.6 liter cylindrical vessel filled with liquid scintillator, two 20 cm conical light guides connected to the ends of the vessel and two low-background photomultiplier tubes to detect scintillator light. In addition, the detector is covered with a reflecting foil. The simulation environment was used to study the energy resolution and intrinsic background of the detector.

The energy resolution of the experiment was simulated for electrons and alpha particles of energies 0-2 MeV ( $e^-$ ) and 3-10 MeV ( $\alpha$ ), which well cover the  $\beta$ -decay energy range of  $^{14}\text{C}$ . In the absence foil, the energy spectrum was highly position-dependent as particles originating near the edges of the vessel yielded more light than particles in the center. As a result, the energy resolution was worse without the foil.

The most prominent source of intrinsic background was gamma rays from the photomultiplier tubes. The liquid bulk consisting of linear alkyl benzene did not cause a noticeable background unless the  $^{222}\text{Rn}$  concentration was of the order of  $1 \text{ Bq/m}^3$  but even still the gamma rays were dominant.

## **ACKNOWLEDGEMENTS**

First I would like to thank Kai Loo for helping me in every step on the way including algorithm design, coding problems, thesis structure, to mention a few. It was the countless meetings and emails that made this work possible. I would also to thank Timo Enqvist for his advice and support in all stages of this work. I truly feel lucky to have this great instructors to help me in this thesis. Finally, I thank the whole CUPP research group for all the support along the way.

## CONTENTS

<b>1</b>	<b>Radioactive decay</b>	<b>8</b>
1.1	Radioactivity . . . . .	8
1.2	Radioactivity as a background source in liquid scintillator detectors . .	10
1.3	External background . . . . .	11
1.4	Intrinsic background . . . . .	13
<b>2</b>	<b>Scintillation in organic scintillators</b>	<b>15</b>
2.1	Passage of radiation through matter . . . . .	15
2.1.1	Heavy charged particles . . . . .	15
2.1.2	Electrons and positrons . . . . .	17
2.1.3	Gamma rays . . . . .	18
2.2	Scintillation process in organic materials . . . . .	20
2.3	Wavelength shifters . . . . .	22
2.4	Response of organic scintillators . . . . .	22
2.4.1	Light yield . . . . .	22
2.4.2	Time response and pulse shape discrimination . . . . .	23
<b>3</b>	<b>C14 Experiment</b>	<b>24</b>
3.1	Experimental setup . . . . .	24
3.2	Location . . . . .	28
3.3	Current status . . . . .	28
<b>4</b>	<b>Geant4 simulation toolkit and simulation setup</b>	<b>29</b>
4.1	Geant4 basic structure . . . . .	29
4.2	Physics implementation . . . . .	30
4.2.1	Radioactive decay . . . . .	30
4.2.2	Optical photon generation . . . . .	30
4.2.3	Photon attenuation . . . . .	31
4.3	Simulation environment for C14 experiment . . . . .	32
<b>5</b>	<b>Simulation results</b>	<b>34</b>
5.1	Energy resolution . . . . .	34
5.2	Background spectra . . . . .	41
5.2.1	LAB background spectrum . . . . .	41
5.2.2	PMT background spectrum . . . . .	45
5.2.3	Comparison with lower $^{14}\text{C}$ concentration . . . . .	45
<b>6</b>	<b>Summary &amp; Outlook</b>	<b>49</b>
	<b>References</b>	<b>50</b>

## INTRODUCTION

The interest in rare-event experiments has been increasing in the past decades as many of the open questions in modern physics can only be addressed by detecting weak signals from the noise. These low event rate experiments include virtually all modern day neutrino physics, for example the study of solar neutrinos [1], [2], double beta decay [3] and dark matter [4]. Solar neutrino experiments focus on the fusion reactions fueling the Sun, as predicted by the standard solar model. One of the fusion products are neutrinos, which are very elusive particles with little interaction with other particles, thus capable of carrying information from the Sun's deep interior. Another field of interest is the study of double beta decay and in particular neutrinoless double beta decay which, if observed, would imply lepton number violation. It is proposed that dark matter comprises of a quarter of the mass and energy in the universe and is composed of weakly interacting massive particles that could be identified indirectly by the emission of neutrinos in pair annihilation of these dark matter particles.

All these studies have common that they typically require huge detector volumes to observe very small event rates. One way of fulfilling this requirement is to use liquid scintillator detectors. Liquid scintillator detector comprises of a liquid that produces light when struck by a charged particle and an apparatus for detecting this light. Liquid scintillator detectors have excellent properties for rare-event experiments, such as high detection efficiency, high transparency, able to be purified and inexpensive cost which is very important as the target volume can be millions of litres. In addition, liquid scintillators allow for particle discrimination and the outer layers of liquid can be used as a buffer to absorb background radiation [5],[6],[7].

Scintillator material in liquid detectors is based on hydrocarbons which usually feature one or more benzene rings responsible for luminescence. The large amount of carbon present in the volume will also result in the presence of radiocarbon  $^{14}\text{C}$ , the radioactive isotope of carbon. Radiocarbon is beta active with half-life of approximately 5730 years. It is primarily created in the upper atmosphere in cosmic ray interaction with nitrogen.  $^{14}\text{C}$  reacts with oxygen to create radioactive carbon dioxide  $^{14}\text{CO}_2$  [8], which then is dispersed with the global carbon cycle to all matter containing carbon, including crude oil which is the source of hydrocarbons in liquid scintillators. The amount of radiocarbon in a material is a function of the material's age given by the universal law of radioactive decay. Since crude oil is millions of years old, the concentration of radiocarbon in scintillators is very low. However, due to large detector mass and extremely sensitive measurements, the decay of radiocarbon will effectively block any signal detection below its endpoint energy of 156 keV [7] or more if there is a pile-up of events. Even with a concentration of  $10^{-18}$ , the rate of  $^{14}\text{C}$  is  $10^5$  times higher than the rate of  $^7\text{Be}$  solar neutrinos [9].

Due to the high  $^{14}\text{C}$  rate, achieving low  $^{14}\text{C}$  concentration would benefit all future neutrino experiments, especially in measuring low energy solar neutrinos. To this end, the C14 experiment in The Pyhäsalmi Mine, Finland, aims to measure the concentra-

tion of radiocarbon of various scintillator materials from different crude oil sources with the aim to find the source with lowest concentration. These measurements are carried out in collaboration with the Baksan Neutrino Observatory [10], where the measurements are being performed as well. Currently, the lowest concentration found is approximately  $2 \times 10^{-18}$ , but the C14 experiment aims to find sources with  $^{14}\text{C} / ^{12}\text{C}$  less than  $10^{-18}$  [11]. In contrast, the required concentration in the upcoming large scale neutrino experiment JUNO [12] for radiocarbon is  $^{14}\text{C} / ^{12}\text{C} < 10^{-17}$ .

In order to better understand the detector setup a simulation environment utilizing Geant4 simulation toolkit is constructed. The simulation environment is suited for the study of detector response, intrinsic background signals, detector geometry optimization and serves as a platform for further simulations of the detector setup. In the present study the detector response for electrons and alpha particles is presented and intrinsic background components from the scintillator sample and the photomultiplier tubes is analyzed and compared against  $^{14}\text{C}$  signal. In addition, the effect of reflective coating in light collection efficiency is discussed. The construction of the simulation environment was also a part of this thesis work.

The structure of this thesis is as follows. Chapters 1 and 2 focus on the theoretical foundation of radioactive decay, radiation interactions with matter and scintillation. Chapter 3 details the detector setup of the C14 experiment. The simulation environment and the detector implementation is presented in Chapter 4. Also, Geant4 simulation toolkit and relevant physics implementation are discussed. The simulation results for the energy resolution and the intrinsic background levels are presented in Chapter 5. Finally, a short summary and outlook is given in Chapter 6.

# 1 RADIOACTIVE DECAY

## 1.1 Radioactivity

An atom comprises of a nucleus and surrounding electrons trapped in a potential well created by the positively charged nucleus. A nucleus holds positively charged protons and charge-neutral neutrons. Since two like charges repel each other, the Coulomb force tries to tear protons in the nucleus apart but the nucleus is held together by the strong nuclear force. However, certain nuclear structures are prone to split in a process called radioactive decay if there is a lower energy configuration that it can achieve through decay. Radioactive decay is a stochastic process, which means it is impossible to predict when a certain atom decays.

Even though the prediction whether a particular atom will decay in a certain time or not is impossible, from a statistical point of view the radioactive decay follows a simple exponential law:

$$N = N_0 e^{-t/\tau}, \quad (1)$$

where  $N$  is the number of nuclei at time  $t$ ,  $N_0$  the original amount of nuclei and  $\tau$  is a time constant characteristic to a nucleus. Other useful quantity when speaking of radioactive decay is half-life which is defined by

$$t_{1/2} = \tau \cdot \ln 2. \quad (2)$$

Half-life represents a duration of time when the amount of radioactive substance is halved. Often it is useful to know how many decays occurs in a certain time frame which is defined as the activity  $A$  of the sample

$$\frac{dN}{dt} = -\tau N, \quad (3)$$

where  $\tau$  is the decay constant. The usually reported unit of activity is Becquerel, defined as number of decays per second, though others exist.

In a radioactive decay process, the nucleus ejects a particle thus becoming a different nucleus. Decay mechanisms are divided into alpha decay, beta decay and gamma decay. In alpha decay, an alpha particle  $\alpha$  is emitted which defined as a  ${}^4\text{He}$  nucleus consisting of two protons and neutrons. The decay mechanism can be written as [13]



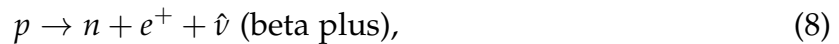
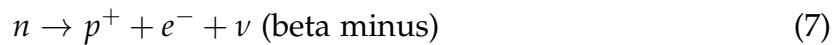
Alpha decay process can be explained through the framework of quantum tunneling. Quantum tunneling says that a particle with a wave-like nature has non-zero probability to be found in classically forbidden areas. In the case of alpha particle, it has a large probability to be found inside the nucleus trapped inside nucleus' potential field, but also a small probability to be found outside nucleus, even though classically it would be impossible. This probability varies from nucleus to nucleus. The momentum of

initial nucleus is zero and so the emitted alpha particle and the daughter nucleus have the same but opposite momentum. Thus the alpha particles have a definite energy depending on the mass of the nucleus and whether the emission of alpha particle leaves the daughter nucleus in the ground state or excited state. As a result, the characteristic alpha decay energy spectrum shows a few distinct spikes corresponding to the different decay energies as seen in the left panel of Fig 1.

The beta decay process is further divided into beta plus and beta minus decay, where in the beta plus decay one of the ejected particle is a positron and in the beta minus decay it is an electron. Decay reactions can be written as



The mass number A does not change in beta decay because the decay is a conversion reaction



where  $\nu$  ( $\hat{\nu}$ ) is a neutrino (antineutrino). The energy spectrum in beta decay is continuous, as in the middle panel of Fig. 1, since the energy is shared between three components: the nucleus, electron (positron) and neutrino (antineutrino). However, the endpoint energy for electron (positron) energy can be determined by letting the neutrino (antineutrino) energy approach zero. If the small recoil energy of the daughter nucleus is ignored, this corresponds to the Q value of the reaction. As in the alpha decay, beta decay can occur either to the ground state or to one of the excited states, and the full beta spectrum is a superposition of all these decay branches.

Third type of decay mechanism is the gamma decay. Analogously to atomic systems, an excited nucleus state decaying into lower state will emit the energy difference as a photon and so the gamma spectrum has distinct spikes corresponding to the difference in energy levels (right panel in Fig. 1). Usually nuclei are in their ground state but often beta or alpha decay will leave the nucleus into excited state, subsequently emitting  $\gamma$  ray, thus usually  $\gamma$  decay follows beta or alpha decay. However, excited nucleus can also relax via internal conversion process, in which the nucleus transfers energy to one of its orbital electrons ultimately ejecting it from the atom. In addition to de-excitation, one other source of gamma rays is the annihilation radiation where an electron and a positron annihilates forming two 0.511 MeV photons emitted at opposite direction with equal momenta.

In many cases, an unstable nucleus decays into another unstable nucleus which in time will decay further. A series of decays following one another is called a decay chain depicted for  ${}^{238}\text{U}$  and  ${}^{232}\text{Th}$  in Fig. 2. Decay chains are important to identify, for example the presence of  ${}^{238}\text{U}$  implies the presence of many other isotopes and thus more decay products. In addition, even though each isotope in the chain has different half-life, in practice the longest half-life dominates the activity of the chain below it. For example in the case of  ${}^{238}\text{U}$  the uranium itself has the longest half-life so it can be approximated that the activity of each isotope in the chain has the activity of the uranium nucleus in question.

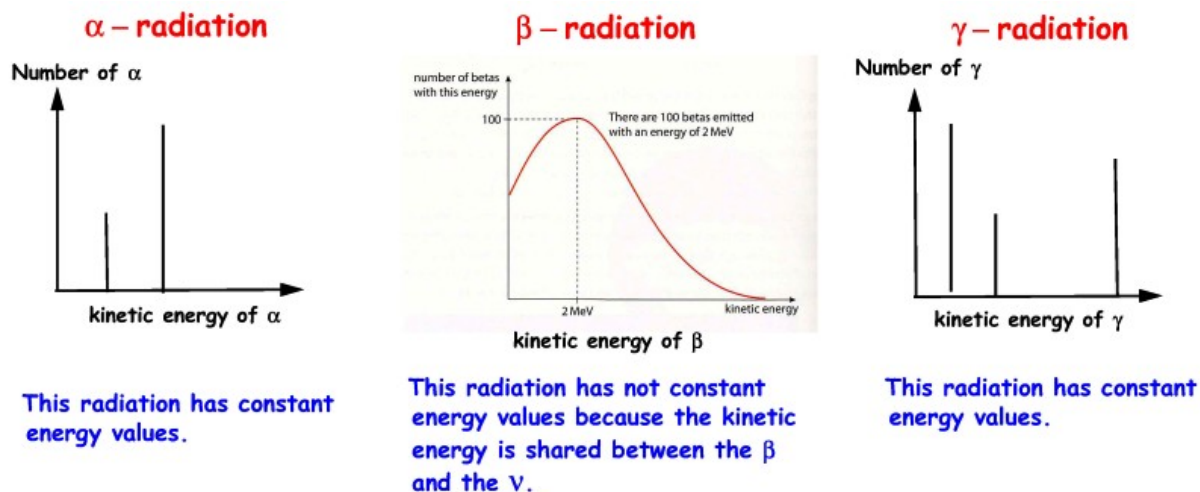


Figure 1: Three graphs depicting the characteristic energy spectrums for alpha, beta and gamma decays<sup>1</sup>.

The energy spectra from emitted particles of different decay types are different. In alpha decay the spectrum consists of one or more sharp peaks each corresponding to the characteristics of the decaying nucleus. Since the process involves only the mother nucleus and the alpha particle, the energy of the alpha particle is always the same. However, the beta decay involves a third particle and the energy is divided with three particles thus the resulting spectrum is continuous between start point and end point energies set by the characteristics of the nucleus. The gamma spectrum has sharp peaks as in the alpha decay since the energy differences in nuclear states are discrete. Schematic representation of these spectra is presented in Fig. 1<sup>1</sup>. However, actual measured gamma and alpha spectra have broader peaks due to the energy resolution of the measurement apparatus and other energy changing processes a particle may come across in its lifetime.

## 1.2 Radioactivity as a background source in liquid scintillator detectors

In experiments with low event rates, minimizing background signal is essential. This is increasingly more important as experiment are getting more and more sensitive. Background sources can be separated into external and intrinsic sources. External sources include cosmic rays and radiation from surrounding materials as well as contaminants in the air. In order to combat the cosmic ray background, most rare event experiments are placed in deep underground laboratories where only muons generated by the air showers are able to reach. Muons are particularly difficult to eliminate from the signal since they create false events not only by direct collisions but also by spallation processes generating radionuclides and fast neutrons to the surrounding materials. Surrounding rock contains omnipresent radionuclides  $^{238}\text{U}$ ,  $^{232}\text{Th}$ , their progenies (Fig. 2) as well as  $^{40}\text{K}$ , all of which generate  $\gamma$ -rays of various energies. Air contains mainly  $^{222}\text{Rn}$  and  $^{85}\text{Kr}$  which can either be dissolved in the scintillator or contaminate detector materials. A careful handling of the detector is thus needed in order to minimize contamination from airborne sources.

<sup>1</sup>[http://perso.numericable.fr/vincent.hedberg/nuclear/nuke\\_sl.html](http://perso.numericable.fr/vincent.hedberg/nuclear/nuke_sl.html)

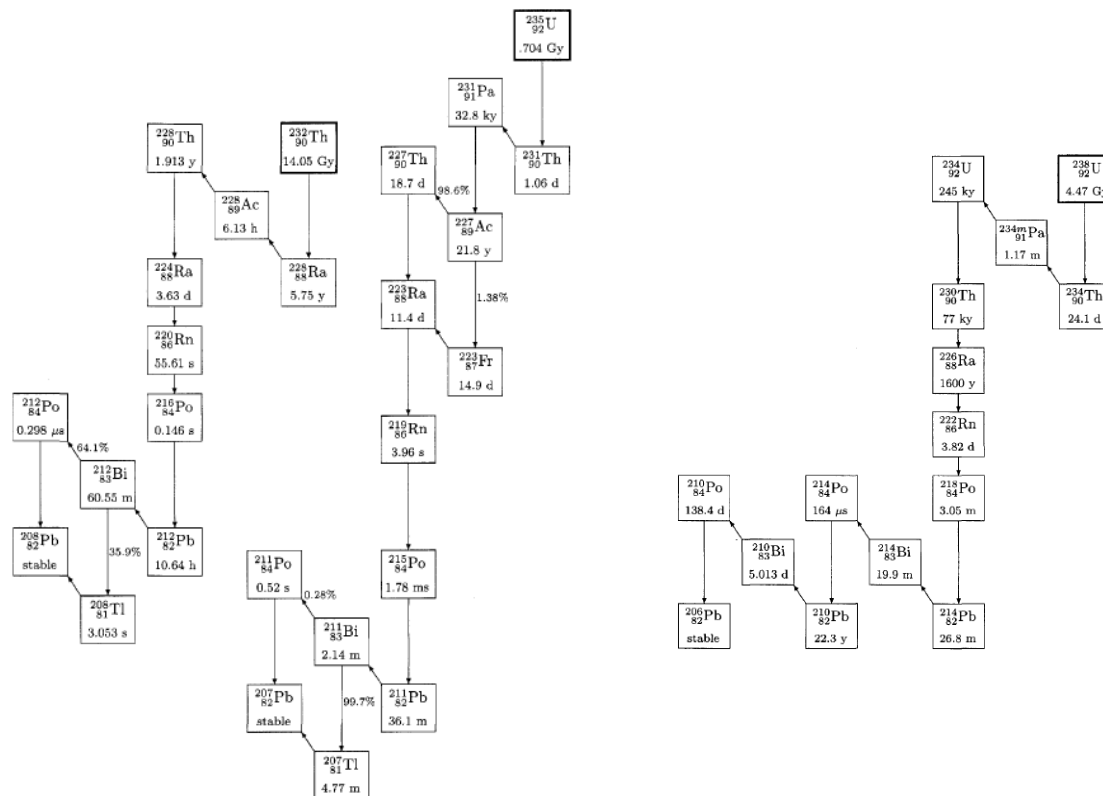


Figure 2: Decay chains for  $^{238}\text{U}$  and  $^{232}\text{Th}$  [14].

Intrinsic sources include radionuclides present in the sample itself or in the detector materials. The most prominent radionuclides typically observed in a liquid scintillator is presented in Tab. 1. Most of the listed isotopes are from either uranium or thorium decay chains as seen in Fig. 2. In addition, there is potassium, krypton and radon from contamination from air and most notably in liquid scintillators there is radiocarbon  $^{14}\text{C}$ , a natural isotope of carbon.

### 1.3 External background

Gamma ray background from surrounding material is almost exclusively coming from the uranium and thorium decay series as well as from decay of  $^{40}\text{K}$ . The main source of these radionuclides in deep underground laboratories is the surrounding rock. In the Pyhäsalmi Mine, the uranium and thorium concentrations are 0.8 ppm and 3.2 ppm, respectively [15]. Air is also contaminated by many radionuclides, most notably  $^{14}\text{C}$ ,  $^{222}\text{Rn}$  with concentration of 1 Bq/m<sup>3</sup> with ventilation [16], and its progenies as well as  $^{85}\text{Kr}$  produced in nuclear fuel processing.

Cosmic rays, consisting mainly of protons and alpha particles, hit the earth atmosphere at rate of approximately  $10^4 \text{ m}^2\text{s}^{-1}$ . These particles interact with atoms in upper atmosphere creating secondary particles, such as protons, electrons, neutrons, pions and muons. As a result, the detector is usually placed deep underground, where only muons can penetrate. This is due to the low ionisation power and considerable larger rest mass than that of electron. Total muon flux at depth of 1400 m (4000 m.w.e.) is approximately  $1.1 \cdot 10^{-4} \text{ m}^{-2}\text{s}^{-1}$  [17]. The penetration length of muons is

Isotope	$T_{1/2}$	Decay mode	$E_{\max}$ [keV]
$^{14}\text{C}$	5730 a	$\beta^-$	157
$^{40}\text{K}$	1.3 Ga	$\beta^-$ (89 %) $\beta^+$ (11 %)	1311 1505
$^{85}\text{Kr}$	10.8 a	$\beta^-$	687
$^{222}\text{Rn}$	3.8 d	$\alpha$	5590
$^{210}\text{Pb}$	22.3 a	$\beta^-$	64
$^{210}\text{Bi}$	5.0 d	$\beta^-$	1162
$^{210}\text{Po}$	138.4 d	$\alpha$	5408
$^{208}\text{Tl}$	3.1 m	$\beta^-$	5001
$^{212}\text{Bi}$	60.6 m	$\beta^-$ (64 %) $\alpha$ (36 %)	2254 6207
$^{212}\text{Po}$	0.3 $\mu\text{s}$	$\alpha$	8954
$^{214}\text{Pb}$	26.8 m	$\beta^-$	1024
$^{214}\text{Bi}$	19.9 m	$\beta^-$	3272
$^{214}\text{Po}$	164.3 $\mu\text{s}$	$\alpha$	7833

Table 1: Most prominent intrinsic background components in a liquid scintillator [7]. Most of these isotopes are a part of  $^{238}\text{U}$  or  $^{232}\text{Th}$  decay chains (Fig. 2).

energy-dependent so the highest energy muons also penetrate the deepest. Still, most of the muons reaching the detector will just pass through. However, they deposit a large amount of energy ( 2 MeV/cm) when interacting with the detector [7].

Another problem with muons is that they are able to generate neutrons and radioisotopes near or in the detector in a spallation process, possibly inducing a background. Most of them created this way are  $^{11}\text{C}$  and  $^{10}\text{C}$  due to the abundance of carbon inside the scintillator. In addition, both thermal and fast neutrons are created by muons in spallation processes. Thermal neutrons are produced when multiple protons are knocked out of nuclei, leaving neutron-rich nuclei such as  $^9\text{Li}$  and  $^8\text{He}$ . Thermal neutrons are emitted in their  $\beta^-$  decay, which are subsequently captured by hydrogen nuclei, further emitting 2.2 MeV gamma rays. It is no surprise that spallation processes can also knock out neutrons out of nuclei, creating energetic fast neutrons as a result. These particles can traverse several meters through materials. Once a fast neutron is thermalized in collisions, it is captured releasing a gamma ray of the order of a few MeV. The total flux of neutrons at the depth of 4000 m.w.e. is approximately  $60 \cdot 10^{-7} \text{ cm}^{-2}\text{s}^{-1}$  [18]. Further, muon induced thermal neutron capture is particularly harmful, as it mimics the signal of inverse beta decay used to detect neutrinos. Usually, the effect of muon flux is minimized by a vetoing process, where essentially the detector is turned off whenever a muon is detected.

## 1.4 Intrinsic background

The most obvious source of intrinsic background is the radioactive components in the scintillator sample itself. When solvents are hydrocarbons, the dominating background component is the  $^{14}\text{C}$ . This omnipresent, radioactive isotope of carbon is primarily formed in the upper atmosphere as nitrogen atoms absorb thermal neutrons [11] in the following reaction:



In most cases, the older the matter is, the lower the concentration of radiocarbon is as it decays with a half-life of 5,730 years. Thus we would expect that oil (a hydrocarbon), being millions of years old, would have a radiocarbon concentration of approximately  $10^{-21}$ , compared to  $10^{-12}$  of fresh material but this is not the case. In fact, we observe concentrations several orders of magnitude larger than expected. More radiocarbon is created in the oil for example by reaction in equation 9, as neutrons coming from local environment reacts with the abundant nitrogen in the oil. Though the concentration of  $^{14}\text{C}$  is still miniscule, in large scintillator experiments  $^{14}\text{C}$  background effectively blocks all neutrino detection below its beta decay endpoint energy of 156 keV. Moreover, due to the pile-up effect along with limited energy resolution, the tail of  $^{14}\text{C}$  spectrum usually stretches to energies well beyond the maximum endpoint energy [16]. Unfortunately, there is no known method of decreasing the radiocarbon in the liquid other than a careful selection of the oil source. Usually, the older and the deeper the source is, the less it has radiocarbon but this is altered by the uranium and thorium concentrations in the local environment.

In addition to  $^{14}\text{C}$ , other radioactive isotopes can be dissolved in the liquid as the sample is being transported or otherwise handled or stored. Most notable impurities acquired this way are  $^{40}\text{K}$ ,  $^{232}\text{Th}$ ,  $^{238}\text{U}$ ,  $^{222}\text{Rn}$  and  $^{85}\text{Kr}$  and their daughter nuclei down the decay chain.

The PMT windows and the scintillator container are made of glass and thus can contain relatively large concentration of radioactive  $^{40}\text{K}$  in addition to the usual contaminants  $^{238}\text{U}$  and  $^{232}\text{Th}$ . The decay of these isotopes produce gamma rays that are capable of reaching the scintillator sample. Since the intensity of the gamma rays is inversely related to the distance squared, the PMT -caused background can be decreased by increasing the distance from the PMTs to the sample.

Intrinsic background sources and their proposed concentrations are listed in Tab. 2. These values are acquired from previous measurements [16],[19],[20], [21],[22] and thus might be slightly different in the present experiment. In Tab. 3 is presented scaled concentration values, all in becquerel, for the C14 experiment.

	$^{238}\text{U}$	$^{232}\text{Th}$	$^{40}\text{K}$	$^{85}\text{Kr}$	$^{222}\text{Rn}$
Scintillator	$10^{-6}$ ppb	$10^{-6}$ ppb	$10^{-14}$ g/g	$50 \mu\text{Bq/kg}$	$1 \text{ mBq/m}^3$
PMT	25 ppb	32 ppb	66 ppm	-	$0.031 \text{ mBq/pc}$
Quartz	$1.2 \text{ mBq/kg}$	$0.01 \text{ mBq/kg}$	$0.04 \text{ mBq/kg}$	-	-
Acryl	10 ppt	10 ppt	10 ppt	-	-

Table 2: Proposed intrinsic background concentrations in different detector components of the C14 experiment, based on previous measurements [16],[19],[20], [21],[22].

	$^{238}\text{U}$	$^{232}\text{Th}$	$^{40}\text{K}$	$^{85}\text{Kr}$	$^{222}\text{Rn}$
Scintillator (nBq)	12.3	4.1	0.31	$70 \cdot 10^3$	$1.57 \cdot 10^3$
PMT (mBq)	82	44	27	-	0.031
Quartz (mBq)	1	0.01	0.04	-	-
Acryl ( $\mu\text{Bq}$ )	80	30	0.20	-	-

Table 3: Background component activities in the C14 experiment scale in Bq.

## 2 SCINTILLATION IN ORGANIC SCINTILLATORS

Scintillation is a phenomenon where a material struck with radiation emits a faint flash of light. The four major radiation categories are presented in Tab. 4. Uncharged radiation has significantly larger attenuation length and can pass through detector unnoticed. Interaction with the detector can produce charged particles such as electrons and alpha particles that can serve as a basis for detector signal. Charged radiation has very small attenuation length thus fully depositing their energy in the medium.

Charged particle radiation	Uncharged radiation
Heavy charged particles	Neutrons
Electrons	X-rays and Gamma rays

Table 4: The four major categories of radiation [23].

### 2.1 Passage of radiation through matter

#### 2.1.1 Heavy charged particles

Heavy charged particles include muons, pions, protons,  $\alpha$ -particles and other light nuclei but excludes heavier nuclei and ions because of the additional interactions that arises with increasing size. Heavy charged particles interact mainly with electrons in the medium through Coulomb force. Though interaction with the nuclei is possible as in Rutherford scattering experiment, it has no significant impact in the context of scintillation detectors. Collisions with electrons will often either excite (raise electron to a higher lying shell) or ionize (knock electron out of the atom) electrons in the medium. As the mass of heavy charged particles are large compared to that of electrons', it requires many collisions in order to stop the particle and the particle's trajectory is fairly straight inside the medium, thus having a well-defined range inside the medium.

**Stopping power** The collisions described above for charged particles are statistical in nature and occur with a quantum mechanical probability. Generally the number of collisions in a track length is large and thus it is meaningful to define a quantity describing the average energy loss of a particle per unit length. This quantity is known as the linear stopping power and is given by

$$S = -\frac{dE}{dx}. \quad (10)$$

It is defined as the differential energy lost per differential path length. An expression for stopping power is known as the Bethe formula [24]:

$$S = 2\pi N_a r_e^2 m_e c^2 \rho \frac{Z}{A} \frac{z^2}{\beta^2} \left[ \ln \left( \frac{2m_e \gamma^2 v^2 W_{max}}{I^2} \right) - 2\beta^2 \right], \quad (11)$$

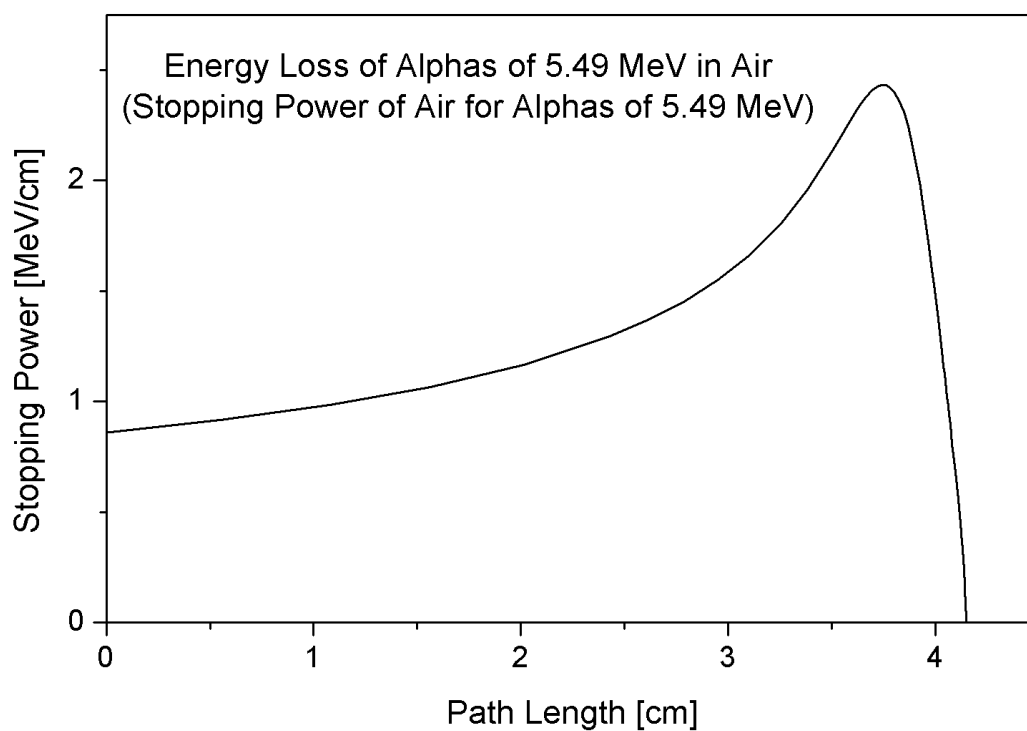


Figure 3: A characteristic energy loss curve of a heavy charged particle known as the Bragg curve. The interaction cross section increases as the particle penetrates the medium, thus increasing the energy loss per unit length. This creates the distinctive peak known as the Bragg peak. From Wikipedia Commons under CC-license.

where  $r_e$  is the electron radius,  $m_e$  the electron mass,  $N_a$  the Avogadro's number,  $W_{max}$  the maximum energy transfer in a single collision,  $I$  the mean excitation potential,  $Z$  the atomic number,  $A$  the atomic weight,  $\rho$  the density,  $z$  the charge,  $\beta = v/c$  and  $\gamma = \sqrt{1 - \beta^2}$ .

In general, the stopping power increases as the velocity of the particle decreases. For a non-relativistic particle, the dependency is  $v^{-2}$ . This originates from the fact that a particle with lower velocity can interact longer with surrounding particles as it progresses through the medium. This is characterized in a Bragg curve, depicted in Fig. 3. The peak of the curve is known as the Bragg peak. For a given velocity, a particle with the highest charge will lose the most energy. Therefore, heavy charged particles have usually shorter path lengths compared for example to electrons as they are heavier (usually lower velocity) and can have larger net charge compared to electrons for example. However, the Bethe formula will fail at low energies as it doesn't take into account the increasing electron interactions in lower velocities, which decreases the effective charge of the particle.

### 2.1.2 Electrons and positrons

As with heavy charged particles, electrons mainly interact with other electrons in the medium. However, as they have equal masses with the particles they collide with, the collisions usually change the momentum of the electrons significantly. For this reason, the path of electrons inside the medium is not straight but quite serpentine. In addition, the definition of range is more vague; electrons traversing the furthest are those with least changed momentum in collisions. Positrons interact in the same way, but with the significant difference in that eventually they will annihilate with electrons, creating two 0.511 MeV photons as products.

**Cherenkov radiation** Cherenkov radiation is electromagnetic radiation produced by a charged particle that travels in a medium with a velocity greater than the speed of light of that medium. A charged particle disrupts the electromagnetic field in the medium and when that particle travels faster than the field can react (due to the limited speed of light in that medium), it creates a shock wave, analogous to sonic boom in supersonic aircraft, emitting coherent radiation.

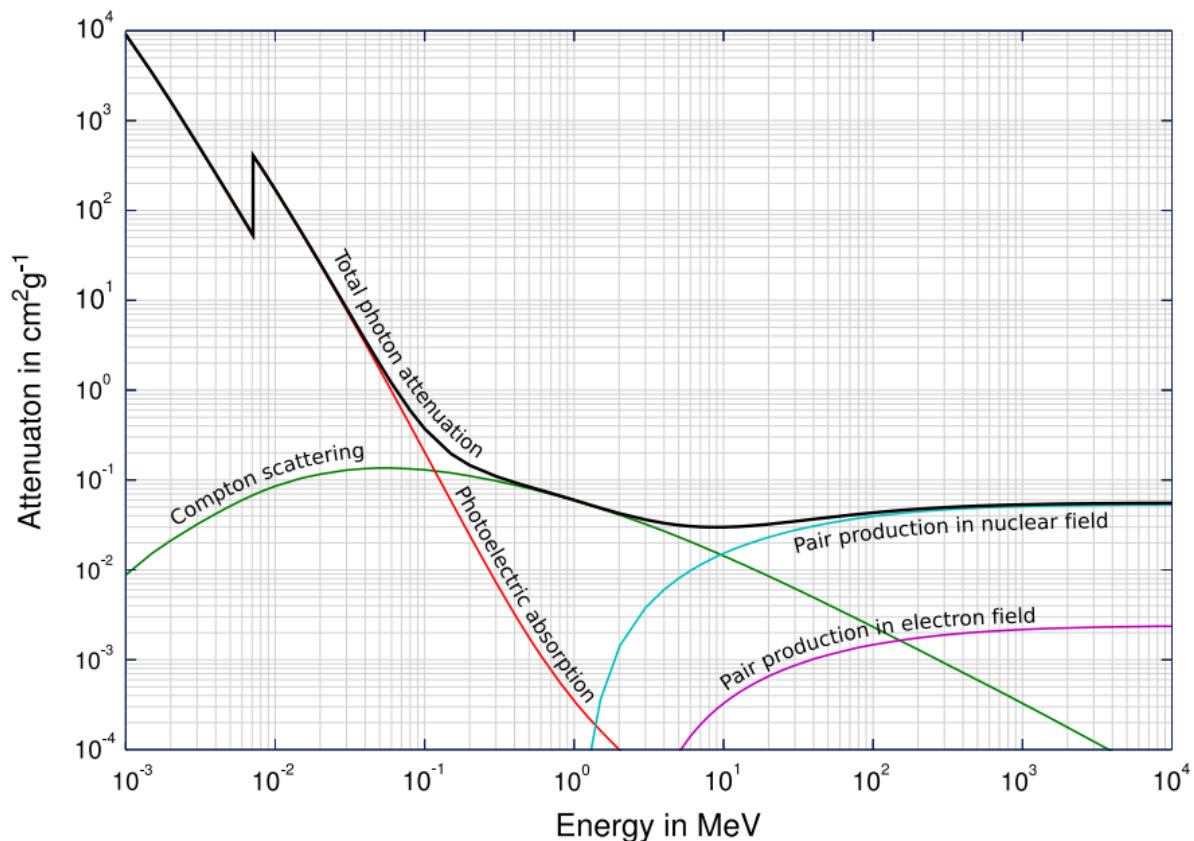


Figure 4: Three main interaction channels of gamma rays with matter: Compton scattering (green), photoelectric effect (red) and pair production (blue and violet). From Wikipedia Commons under CC-license.

## Bremsstrahlung

A charged particle experiencing deceleration emits photons with continuous spectrum labelled bremsstrahlung or "braking radiation". While this can occur for any charged particles, it is vastly more probable for electrons and positrons than for any other charged particle.

### 2.1.3 Gamma rays

The interaction of gamma rays with matter is divided into three main forms of interaction: photoelectric effect, Compton scattering and pair production. All of these interactions have in common that their cross section is small relative to charged particles and the photon is converted into energy. As a result, the gamma rays are more penetrating than charged particles and surviving photons have not lost any of their energy. Probability for each interaction is dependent on the energy of the photon, though usually photoelectric effect dominates in low energies, pair production in high energies and Compton scattering in between, as is shown in Fig. 4.

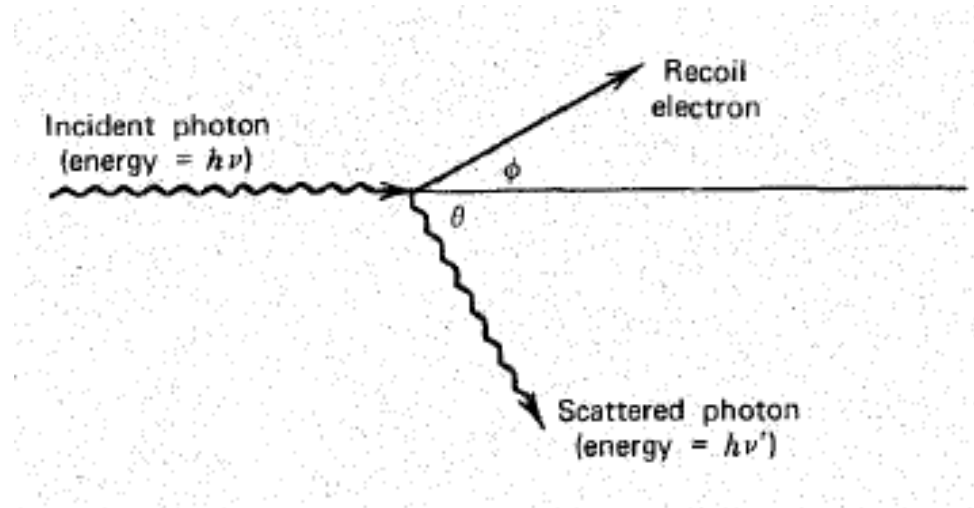


Figure 5: Compton scattering. Incident photon is scattered from the electron with an angle  $\theta$  [23].

**Photoelectric effect** A photoelectric effect is an interaction where a photon is being absorbed by an atom, following an ejection of a photoelectron. The energy of the ejected electron is given by

$$E = h\nu - E_b, \quad (12)$$

where  $E_b$  is the binding energy of the electron. Binding energy is the energy needed to remove the electron from the atom. This interaction can only occur with electron bound to a nucleus. In addition, the interaction leaves an ionized atom with an electron deficit which is quickly resolved either by a capture of an electron or by rearrangement of its remaining electrons which may further result in the emission of one or more photons.

**Compton scattering** Compton scattering is a scattering of a photon from an electron. Incoming high-energy photon is deflected with an angle  $\theta$  and transfers a portion of its momentum to the electron. The electron can be considered free since the energy of the incoming photon is much larger than the binding energy of the electron. Using energy and momentum conservation laws, the energy of the scattered photon can be written as

$$E'_p = \frac{E_p}{1 + \frac{E_p}{m_e c^2} (1 - \cos\theta)}, \quad (13)$$

as is shown in Fig. 5.

**Pair production** In the process of pair production, a gamma-ray photon transform into an electron and a positron. For this to be possible, a gamma-ray photon must have energy over 1.022 MeV, twice the rest mass of an electron or a positron. In addition, this requires the photon to be in a Coulomb field of the nucleus.

## 2.2 Scintillation process in organic materials

Luminescence is a process where a material emits visible light following an absorption of radiation usually of higher energy than the emission. It stems from the electronic structure of the molecules which is usually dictated by the structure of carbon in organic molecules. Carbon has an electron configuration  $1s^2 2s^2 2p^2$ , which means that carbon has four valence electrons in the 2s and 2p orbitals available for binding with other atoms. These atomic orbitals form new hybrid orbitals with three alternative configurations known as  $sp^3$ ,  $sp^2$  and  $sp$  hybrid orbitals. Among these, the  $sp^2$  and  $sp$  orbitals are capable of forming  $\pi$ -bonds, which excited states are responsible for luminescence in organic molecules [25].

A typical level diagram for organic molecule containing  $\pi$ -bonds is shown in Fig. 6. Energy levels are denoted with  $S_{XY}$  or  $T_X$ , where S and T stand for singlet or triplet spin state, and the subscripts X and Y stand for electronic and vibrational levels, respectively. There are multiple vibrational energy levels for each electronic singlet state, giving rise to the fine structure of an electron energy level. The energy spacing between electron levels in organic molecules is usually of the order of 3-4 eV, while the vibrational levels are a few tenths of an eV apart. Because the average thermal energy for molecules at room temperature is around ten times less than the spacing between vibrational levels, almost all molecules at room temperature are at their ground state  $S_{00}$ . All higher level electronic singlet states such as  $S_2$  will de-excite very quickly (in the order of picoseconds) back to the first electronic excited state  $S_1$  through radiationless internal conversions. Moreover, any state with excited vibrational state will also quickly de-excite back to its ground vibrational state. The outcome is that an excited organic material will have a population of excited molecules at the  $S_1$  state. This also explains why the scintillator is transparent to its own fluorescence. Because of the radiationless transformations, for the most part the molecules absorb photons with more energy than they emit. This difference in absorption and emission maxima is known as the Stokes shift.

The three main ways an organic molecule exhibits luminescence are fluorescence, phosphorescence and delayed fluorescence. The origin of all three processes is depicted in Fig. 6. The primary scintillation light comes from the fluorescence, where an excited  $S_1$  state de-excites into the ground state. If the decay time from  $S_1$  to  $S_0$  is  $\tau$ , then the fluorescence intensity is given by

$$I = I_0 e^{-t/\tau}. \quad (14)$$

In most cases,  $\tau$  is a few nanoseconds. The fluorescence spectrum comes from the transitions from  $S_1$  to various vibrational levels  $S_{01}$  and such. Phosphorescence, differs from the fluorescence in longer decay time (approximately  $10^{-4}$  s) and it has longer wavelengths. Phosphorescence may occur if the triplet state T becomes occupied in radiationless transition from  $S_1$  state and then decays to the ground state. If the triplet state acquires sufficient energy, it can transition back to  $S_1$  state followed by a decay

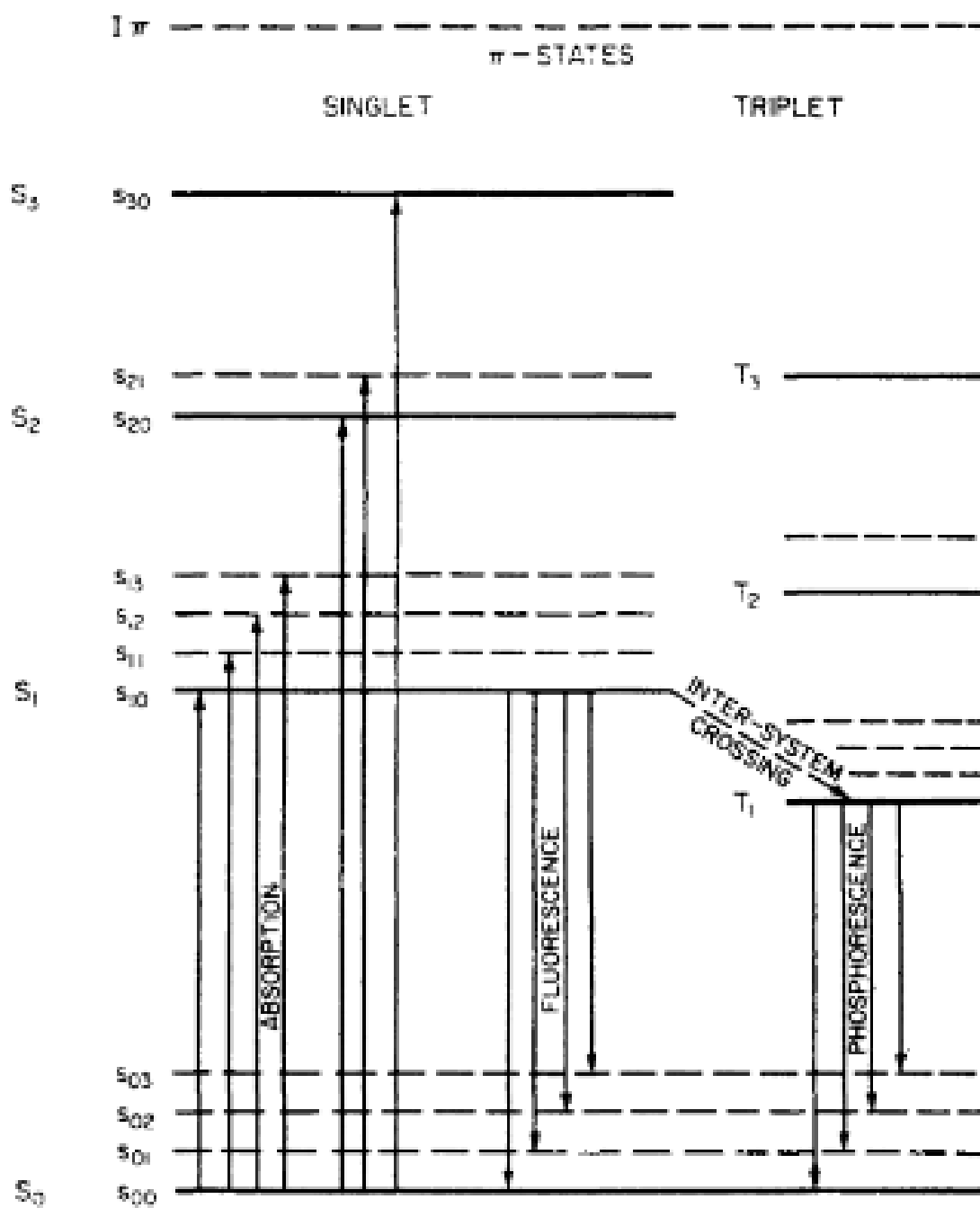


Figure 6:  $\pi$ -energy levels of an organic molecule [25].

into the ground state. This process is called delayed fluorescence and is characterized by the same emission spectrum as in fluorescence but with much longer decay time due to transitions between metastable triplet states.

## 2.3 Wavelength shifters

Even though there is a Stokes' shift between absorption and emission spectra, they heavily overlap [7]. This decreases the efficiency of the scintillator. To this end, scintillator liquids (solvents) are doped with wavelength shifters which are solutes that, as the name implies, shift the emission spectra wavelength. The emitted light is now not re-absorbed by the detector volume itself. The wavelength shifter molecules capture the energy of the solvent's excited states but due to their properties, the process is irreversible. The excited solute molecules can only release the captured energy as photons [27]. Only a few grams per liter of solute is needed to achieve maximum light yield. Another important role of the wavelength shifters is to shift the emission wavelength closer to the optimal detection efficiency wavelength of the photomultiplier tubes.

## 2.4 Response of organic scintillators

### 2.4.1 Light yield

Only a small fraction of the radiation energy deposited in a scintillator is converted to light. This conversion efficiency from energy deposited to light emitted is known as the light yield. This is a key factor in the performance of a scintillator detector. Generally, this quantity varies between particle types and scintillator materials. For example, the light yield is less for heavy charged particles than it is for electrons. The response of organic scintillators was described by Birks [25] in terms of  $dL/dx$ , the light yield per unit length and  $dE/dx$ , the energy lost per unit length, first in 1951. In his work, he argued that the deviations in light yield is caused by quenching of the excited molecules along the track of the particle leading to lowered scintillation efficiency. Assuming that the quenching is directly proportional to the energy of the radiation with a proportionality constant  $B$ , and that it happens with a certain possibility  $k$ , the effect of quenching can be written as  $kB(dE/dx)$ . Furthermore, if we assume that in the absence of quenching the light yield is directly proportional to the specific energy loss, this leads to

$$\frac{dL}{dx} = \frac{A dE/dx}{1 + kB dE/dx} \quad (15)$$

known as the Birks' law. For example, in the case of electrons,  $dE/dx$  is small, and Birks' formula predicts that

$$\frac{dL}{dx} \approx A \frac{dE}{dx} \quad (16)$$

i.e. the light yield is linearly dependent of the energy deposited. However, if  $dE/dx$  is large, as in the case of alpha particles, we have

$$\frac{dL}{dx} \approx \frac{A}{kB} \quad (17)$$

so the formula predicts a saturation point above which the light yield cannot increase.

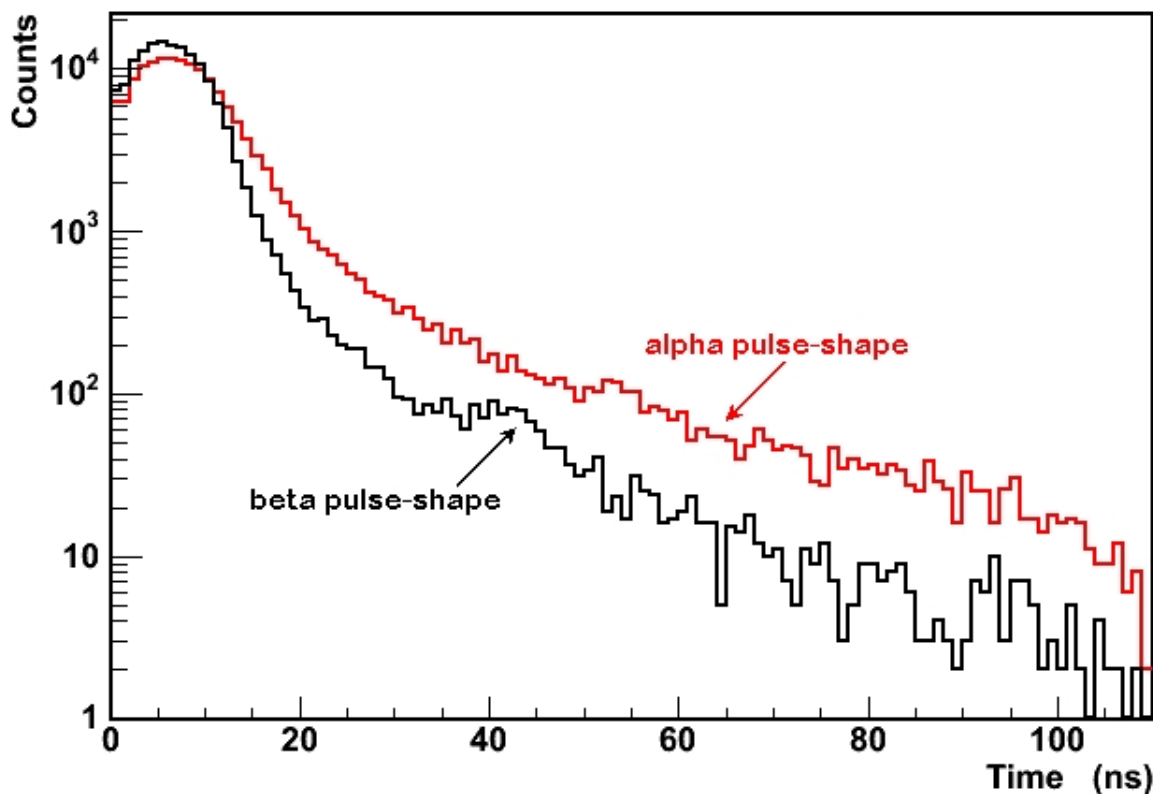


Figure 7: Example of pulse shapes seen for electrons and alpha particles. The difference in these shapes allows for discrimination between different incident particles [26].

#### 2.4.2 Time response and pulse shape discrimination

Even though a prompt fluorescence is a very fast process, it is not instantaneous. The population of excited states takes up approximately half a nanosecond and, depending on the molecule, a further few nanoseconds passes in the decay process. One way to take these two steps into account is to use exponential model for the light pulse

$$I = I_0 \left( e^{-t/\tau_1} - e^{-t/\tau_2} \right), \quad (18)$$

where  $\tau_2$  is the time constant for the population and  $\tau_1$  for the decay.

Most of the scintillation light comes from the prompt fluorescence but also delayed fluorescence and phosphorescence play a role. Their decay time are much longer than of prompt fluorescence. Hence the total pulse shape can be expressed as a combination of fast component and a slow component. The ratio of these components depends on the incident radiation type, setting a basis for pulse shape discrimination, a separation of incident radiation when their energy deposits are equal (Fig. 7).

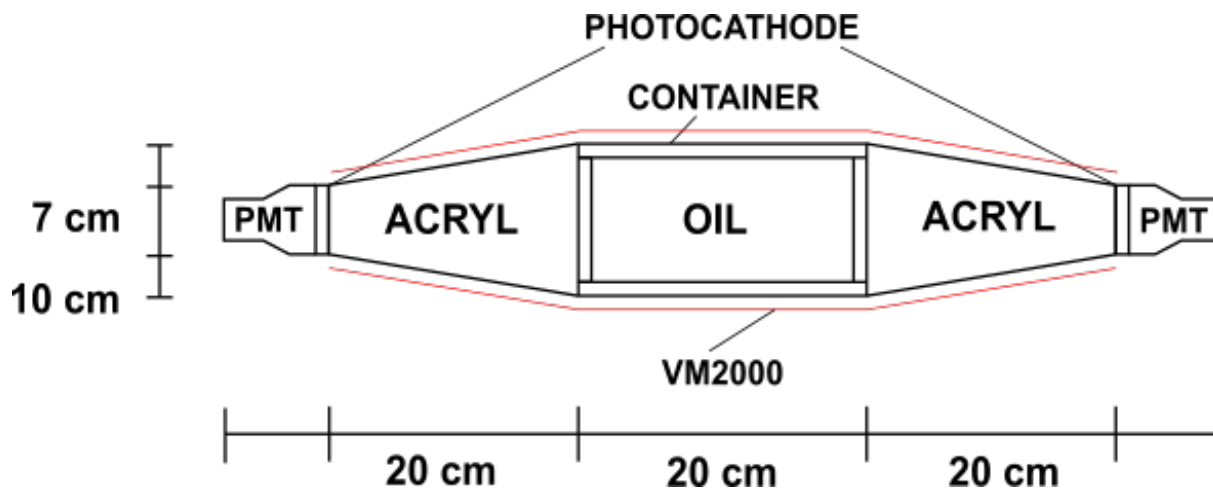


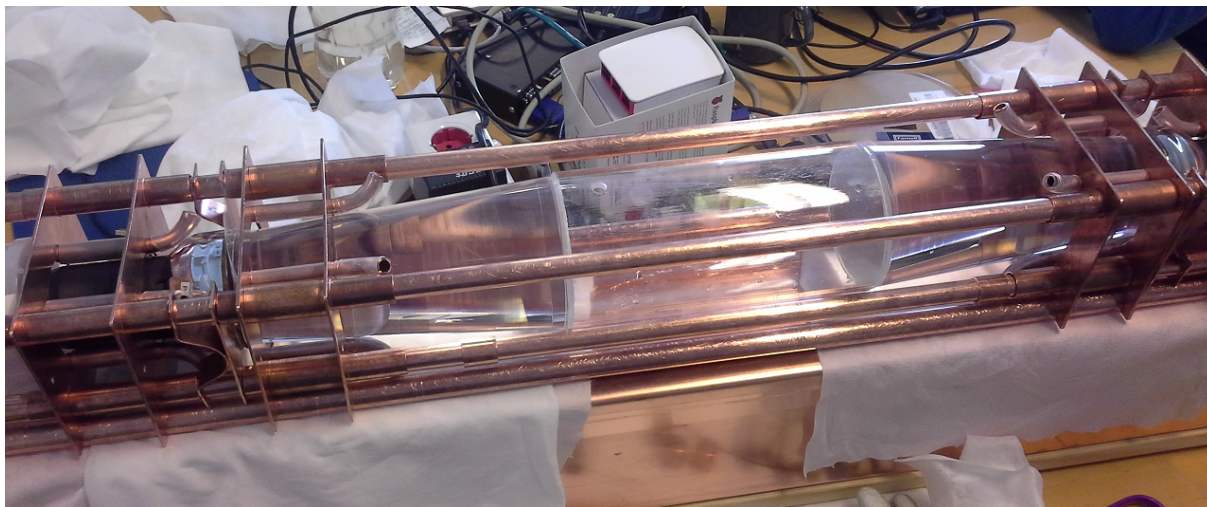
Figure 8: Schematic picture of the C14 experiment geometry. Approximately 1.6 liter cylinder is filled with liquid scintillator. In both ends of the cylinder are two conical acrylic light guides which direct light to the photomultiplier tubes (PMT). The detector is covered with highly reflective VM2000 foil (red).

### 3 C14 EXPERIMENT

The  $\beta$  decay from  $^{14}\text{C}$  is a central background source in a large-scale scintillator experiments and finding a solvent sample with the least amount is vital in optimizing the measurement. There is variance in the amount of radiocarbon between different scintillator samples, depending on the source of crude oil from which the sample was produced from. In addition, the surface contamination of the transportation and storage containers potentially increases radiocarbon in the sample. To this end, a  $^{14}\text{C}$  concentration measurement has been set up to the deep underground laboratory Lab 2 in the Pyhäsalmi Mine, Finland. The aim for the measurement is to observe a scintillator sample with the least amount of  $^{14}\text{C}$ , preferably in the  $^{14}\text{C}/^{12}\text{C} = 1 \cdot 10^{-18}$  level or lower.

#### 3.1 Experimental setup

The detector geometry is presented in Fig. 8. The volume of the cylindrical container in the middle is approximately 1.6 liters and has a radius of 5 cm. The container is made of quartz and filled with linear alkyl benzene (LAB), doped with fluor PPO (Table 5, Figure 10). The light guides in the sides are acrylic and the whole detector is covered in highly reflective VM2000 (specular reflecting multi-layer polymer) foil in order to enhance light collection. This setup is nearly identical to what has been previously been used to study the  $^{14}\text{C}$  concentration [10],[28]. The detector lies upon a copper structure and the setup is covered in multiple 5 cm layers of lead and copper in order to minimize external background radiation (Fig. 9b). In addition, the central part is planned to be flushed with nitrogen in order to minimize radon background [29].



(a) The detector setup.



(b) Base upon which the detector is placed. The detector is to be covered in multiple 5 cm layers of lead and copper in order to minimize external background radiation.

Figure 9: The implementation of the detector and its base.

Solvent	LAB	PPO
Chemical formula	$C_{18}H_{30}$	$C_{15}H_{11}NO$
Molecular weight [g/mol]	241	221
Density	$863 \text{ kg/m}^3$	-
Refractive index	1.49	-
Absorption maximum [nm]	260	303
Emission maximum [nm]	283	365
Attenuation length	$\sim 20 \text{ m}$	-
Scattering length	$\sim 25 \text{ m}$	-

Table 5: Relevant properties of linear alkyl benzene (LAB) [30] and fluor 2,5-Diphenyl oxazole (PPO) [30],[31].

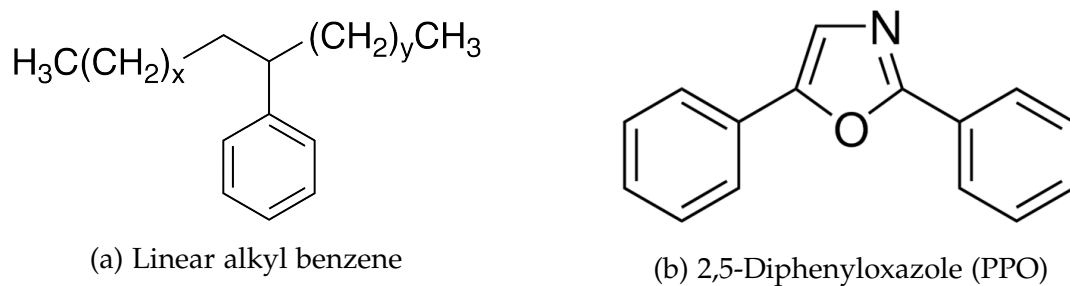


Figure 10: Molecular structures of the scintillator molecules used in the experiment. Linear alkyl benzene (LAB) makes up the bulk of the solution and is doped with 2,5-Diphenyloxazole (PPO) of a few grams per litre. Both molecules have a benzene ring responsible for luminescence in organic scintillators.

Photomultiplier	ET 9302B
Active diameter	70 mm
Quantum efficiency maximum	30 %
Spectral range	285 - 630 nm
Refractive index	1.49
Gain	$1 \cdot 10^7$ (1150 V)

Table 6: Characteristics of the ET 9302B low-background photomultiplier tubes [32].

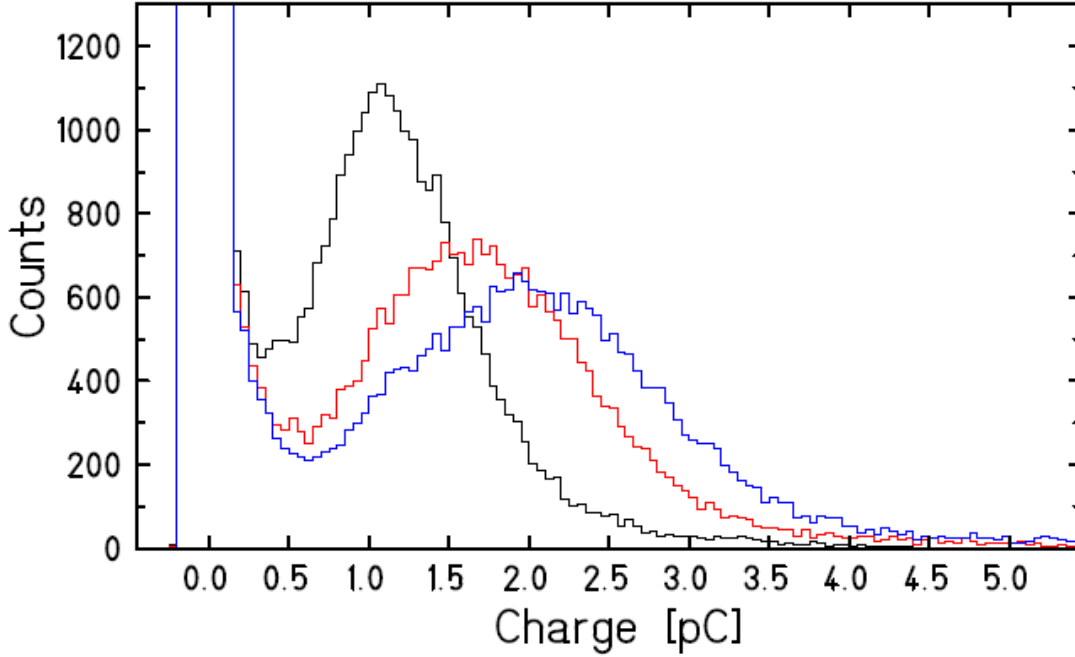


Figure 11: Calibration spectra of the 3" ET9302B low-background photomultiplier tubes. The voltages are 1100 V (black), 1150 V (red) and 1175 V (blue) with the gain being  $10^7$  at 1150 V.

Photomultiplier tubes used in this experiment are ET 9302B 3" low-background tubes. Their characteristic properties are presented in Tab. 6. The maximum quantum efficiency wavelength is close to the emission maximum of PPO (365 nm) thus we can expect the quantum efficiency to be close to the maximum with this setup. The photomultiplier window is made of borosilicate glass which background levels are presented in Tab. 2. The calibration of ET9302B tubes has been carried out and an example of the results are presented in Fig. 11. A gain of  $10^7$  is observed when the voltage is 1150 V. Data acquisition setup consists of a DRS4 evaluation board connected directly to the PMTs. The DRS4 samples the pulse in 1024 bins of the width of 0.2 ns with the maximum sampling speed of 5 GS per second [29].

### 3.2 Location

The detector is being built in the Pyhäsalmi Mine, Finland, at deep underground laboratory Callio Lab [15]. Near the bottom of the mine, at the depth of approximately 1430 m (4100 m.w.e.) is a newly built experimental hall Lab 2 that hosts this experiment. It has floor area of 120 square meters and it is approximately nine meters high. The walls of the laboratory are covered in 5 cm thick layer of shotcrete with activities  $^{40}\text{K} = 140 \text{ Bq/kg}$ ,  $^{226}\text{Ra} = 160 \text{ Bq/kg}$  and  $^{232}\text{Th} = 240 \text{ Bq/kg}$ , whereas the floor is made of low activity concrete. The air quality compares to a normal office air quality and the airflow is designed such a way that it keeps the air from the mine entering the laboratory, thus offering protection from airborne impurities.

### 3.3 Current status

The experimental setup has been underground for about two months. The shielding (Pb and Cu) has been added layer by layer (5 cm per layer). Currently (middle of December), there is 5 cm of copper and 10 cm of lead. The trigger rate is approximately 1.3 Hz (with trigger of PMT1 AND PMT2, thresholds at -16 mV and gain  $10^7$ ). The VM2000 foil has not yet been installed. Before doing so, the gain needs to be lowered to prevent pulse overflows. Measurements with smaller gain are started before the Christmas and the foil is installed in January 2017.

## 4 GEANT4 SIMULATION TOOLKIT AND SIMULATION SETUP

Geant4 [33] is a simulation toolkit designed to study the passage of particles through matter. Its object-oriented and modular design allows for a flexible and highly customizable setup with great transparency and room for implementing user-defined processes. In addition, Geant4 features an abundant set of physics processes for numerous interactions and energy scales.

### 4.1 Geant4 basic structure

On the top of the hierarchy is the run module. It is a collection of events that share the same detector conditions and physics processes. Invoking the BeamOn command will initiate the event loop and the simulation begins. In the beginning of an event, primary particles are being generated and pushed onto a stack. An event ends when there are no particles in the stack. A particle's current information (position, momentum etc.) as well as static information (mass, charge etc.) is stored in a track object. This information is updated as particle traverses in the simulation. The movement of a particle is handled via step module where also physics processes are implemented. Each particle has its own list of applicable physics processes, e.g. radioactive decay. At each step, for every applicable discrete and continuous process a step length is being calculated. The process with the smallest step length is invoked along with any continuous processes. In Geant4 architecture, moving of the particle is also a process, which step length equals to the distance to the next volume boundary. Physics processes may also produce secondary particles that are being pushed onto the stack.

In order to construct a simulation environment, the user must implement user initialization and action classes. As the names suggest, the user initialization classes are invoked at the initialization stage of the simulation, i.e. before a run is initiated. Equally, the action classes are invoked during the run. The UserDetectorConstruction initialization class is where the geometry and the materials are defined. Another important initialization class is UserPhysicsList which holds all the physics processes implemented in the simulation. It is not possible to have an algorithm that could model the entire scope of interactions so user must define a list of processes most suitable for the simulation. However, Geant4 provides physics modules that contains all relevant physics processes in a certain category, e.g. optical physics, to compose physics list from such modules. User action classes are used to define additional procedures inside the event loop. In most cases, they are used to collect and record data and to enhance the performance of the simulation. For example, they can be used to kill any secondary particles or store the energy of a particle created in radioactive decay.

## 4.2 Physics implementation

In the following section the implementation of selected key physics processes most relevant for the present study is highlighted.

### 4.2.1 Radioactive decay

Radioactive decay processes are simulated in the Geant4 toolkit employing data from the ENSDF [34], which contains information for example on half-lives, decay types and emission energies. It is maintained by the National Nuclear Data Center and is considered the standard for nuclear structure and radiation data. For  $\beta$ -decay, which has a continuous spectrum, the spectrum is sampled through Fermi  $\beta$ -function [35]

$$N(p)dp = F(Z,E)p^2(E_0 - E)^2dp, \quad (19)$$

where  $p$  is the momentum,  $E_0$  is the end-point energy,  $E$  the total energy of a  $\beta$ -particle and  $F(Z,E)$  is the Fermi correction factor

$$F(Z,E) = \left[ \frac{A+B}{E-1} \right]^{1/2}, \quad (20)$$

where  $Z$  is the atomic number,  $E$  is the  $\beta$ -particle energy and  $A$  and  $B$  constants. In the simulation, the  $\beta$ -energy distribution is calculated first, from which the  $\beta$ -particle energy is drawn. Simulated  $^{14}\text{C}$   $\beta$ -decay electron energy spectrum using equations 19 and 20 is presented in Fig. 12.

### 4.2.2 Optical photon generation

In the Geant4 simulation framework, optical photons are considered distinct from gamma particles. This allows for implementation of wave-like behavior incorporated into the physical processes. Note that optical photons are created without energy conservation. In Geant4, the processes that create optical photons are Cerenkov effect, scintillation and radiation transition.

**Cerenkov effect** A particle emits Cerenkov photons with an angle

$$\cos\theta = \frac{1}{\beta n}, \quad (21)$$

where  $\beta$  is the speed  $v/c$  and  $n = c/c'$ , where  $c'$  is the group velocity of light in the material. The number of photons created per track length is given by

$$\frac{dN}{dx} = 370z^2 \left[ \epsilon_{max} - \epsilon_{min} - \frac{1}{\beta^2} \int_{\epsilon_{min}}^{\epsilon_{max}} \frac{d\epsilon}{n^2(\epsilon)} \right], \quad (22)$$

where  $\epsilon$  is the photon energy. The number of photons created in a step is calculated from a Poisson distribution with  $\langle n \rangle = \text{step length} \cdot dN/dx$ . Finally, the energy distribution of the photon is acquired from the density function

$$f(\epsilon) = \left[ 1 - \frac{1}{n^2(\epsilon)\beta^2} \right]. \quad (23)$$

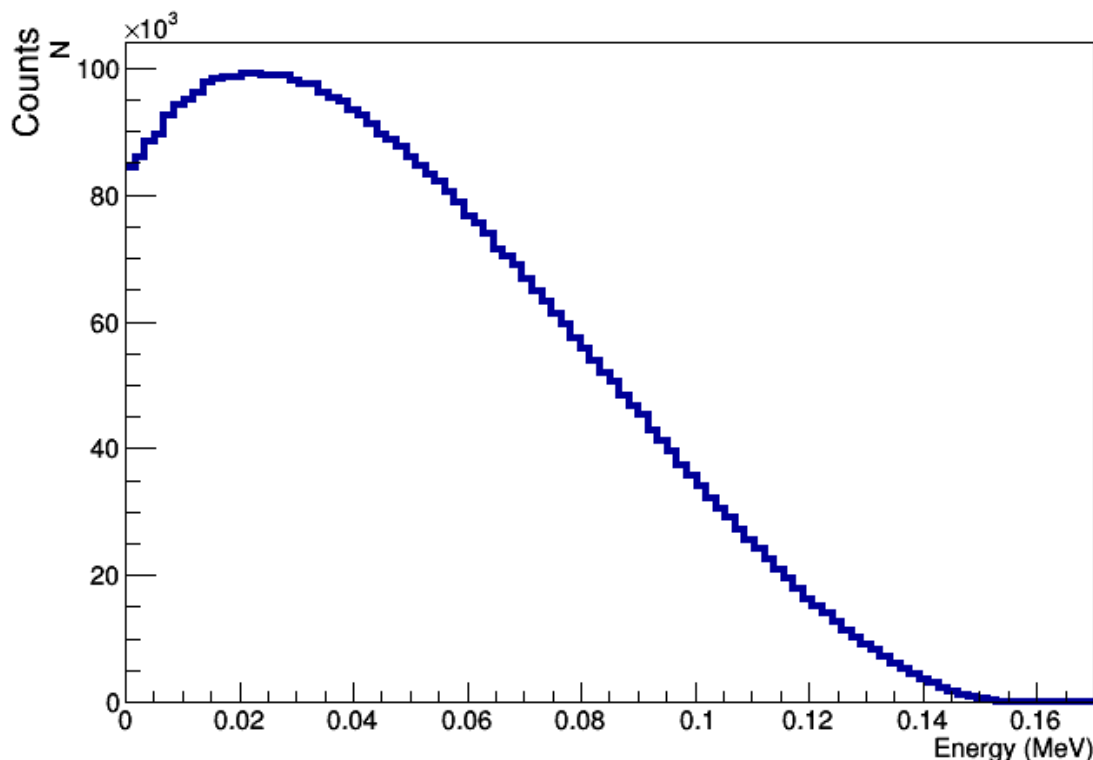


Figure 12: The beta decay electron energy spectrum of  $^{14}\text{C}$ , simulated with Geant4 radioactive processes.

**Scintillation** The generation of scintillation photons is sampled from a Poisson distribution. The average number of scintillation photons is calculated from the light yield, Birks' constant and yield factor, all specified by the user, as well as energy deposited per track length which is calculated in the simulation. For time distribution, an exponential model is used with fast and slow components again specified by the user. Angular distribution is isotropic with a random linear polarization.

#### 4.2.3 Photon attenuation

Optical photon absorption is implemented simply by terminating photon track if its track length exceeds absorption length specified by the user. Rayleigh (elastic) scattering is processed from user defined Rayleigh scattering length, which is the average distance a photon travels in the medium before it is Rayleigh scattered. The scattering angle  $\theta$  is sampled from a distribution given by

$$\Phi(E,\theta) = [1 + \cos^2\theta]\sin\theta \times FF^2, \quad (24)$$

where  $FF$  is the form factor [36] extracted from evaluated data set for a given material.

The third type for altering the path of an optical photon in Geant4 is in boundary processes. The handling of the process depends on the type of materials that join at the boundary. In the case of two dielectric materials, the possible interactions are reflection or refraction, depending on the photon's wavelength, angle of incidence, refractive indices of the materials and the linear polarization of the photon. In the case of dielectric - metal surface, possible interactions are reflection or absorption.

Moreover, Geant4 provides a concept of a surface, for which user can specify properties and parameters, for example reflectivity, refraction index and ruggedness, in order to simulate properties of real-world boundaries. For some common surface treatments (e.g. ESR film, Teflon) Geant4 incorporates their properties into its code in the form of Look-up-tables [37].

### 4.3 Simulation environment for C14 experiment

The simulation environment is based on the Geant4 simulation toolkit version 4.10.01 and was written by the author.

In Geant4, materials are constructed by assigning their elements with relative weights and the density of the material. Each material also has a material properties table, in which the user can define specific parameters which are then used in calculating physics processes. For example, by defining an absorption length in the material properties table, each optical photon traversing through the material now has a probability of being absorbed in the material at a given step based on this parameter.

Detector geometry is depicted in Fig. 8 and is identical to presented in section 3.1. All material properties are user-defined and presented in Tab. 7. VM2000 [37] foil covering the detector was implemented by placing a thin aluminum surface around the detector setup and then defining an optical surface in aluminum boundary through look-up-tables. More specifically, a `groundvm2000air` option was used to make the foil surface rugged. This did slightly randomise the reflection angle of photons as to mimic real world behavior. The simulation assumes 98.5 % reflectivity of the VM2000 foil, thus implying a 1.5 % probability for absorption in the surface per photon collision.

A modular physics list was employed in this simulation. The modules chosen were `G4DecayPhysics`, `G4RadioactiveDecayPhysics`, `G4EmStandardPhysics` and `G4OpticalPhysics`. List covers phenomena related to radioactive decay, electromagnetic interactions and optical physics, i.e. all possible interactions relevant in this experiment. As an example, the decay chains of  $^{238}\text{U}$  and  $^{232}\text{Th}$  are long and contain many radioactive isotopes but using physics modules, Geant4 automatically includes all the decay properties of these isotopes, including decay chains and decay energies with corresponding distributions.

Hit detection was implemented through a concept of a sensitive detector. Once a geometrical object is declared as a sensitive detector, it will register a hit when a particle exits its geometry. In this simulation, the sensitive detectors are the photomultiplier tubes' front surfaces. Moreover, a hit is registered only if the particle hitting the detector is a photon. All photon hits are registered and the quantum efficiency of the real photomultiplier tubes is taken into account later in the analysis. The data acquisition setup was not simulated.

Geant4 doesn't provide any values for optical properties so this was up to user to define correct values for realistic output. The key optical parameters used in this simulation for LAB is presented in tables 7 and 8. These values were mainly taken from the LENA [30] simulations' source code.

	Refractive index	Absorption length (m)
LAB	1.484	20
Glass	1.490	4.2
Acryl	1.500	5
Quartz	1.450	4

Table 7: Refractive indexes and absorption lengths assigned to materials used in the simulation.

	LAB
Rayleigh scattering	40 m
Resolution scale	1
Yield ratio	0.72 (electrons), 0.55 (alpha particles)
Light yield	10000 / MeV
Fast time constant	3.7 ns
Slow time constant	31 ns
Birks' constant	0.15 mm / MeV ( $e^-$ ), 0.107 mm / MeV ( $\alpha$ )

Table 8: Optical parameters of LAB used in the simulation.

	Energy range (MeV)	Step size (keV)
Electrons	0 - 2	20
Alpha particles	3 - 10	100

Table 9: Energy ranges and step sizes used in the energy resolution simulation.

## 5 SIMULATION RESULTS

The constructed simulation environment was employed to predict the energy resolution of the C14 detector and the intrinsic background spectra caused by the detector materials. The simulations were run with and without the VM2000 foil to identify the worst and the best case scenarios for the detector response.

### 5.1 Energy resolution

The aim of energy resolution simulations was to determine the detector light output in LAB filled container for electrons, alpha particles and positrons with energies up to 10 MeV for alpha particles and 2 MeV for electrons and positrons. Light output per energy deposited is called the energy response of the detector and is unique for each detector setup, as it is influenced by things such as the light yield of the scintillator, the type of the particle and the geometry of the setup, for example. The width of the energy response curve is referred as the energy resolution, usually measured as a ratio of the width of the peak to the mean. Better (smaller) energy resolution means more accurate measurements and requires less data to be gathered in order to obtain meaningful results. Here the energy response was determined by simulating 5000 events (one event equals one created particle) for each energy throughout the energy range (Tab. 9), randomly distributed inside the liquid. The light produced, measured by the number of photons reaching PMTs, from each event were recorded in a one-dimensional histogram.

In figures 13 and 14, the energy response of electrons and alpha particles with and without the VM2000 coating is presented. The colors represent the density of events. What immediately strikes out is the spread of the events when the coating is not used. Without coating, the energy response curves show two distinct peaks (Fig. 17a), most notably visible in the alpha particle case. This implies poor energy resolution. However, this is not seen when the coating is implemented. Especially for electrons the curve is very concise. The bumps in the alpha particle case are an artefact of the simulation engine and not expected in actual experiment. In addition, there are no bumps in the  $^{14}\text{C}$  energy range and thus the bumps have no impact to the results.

The implementation of VM2000 foil yielded energy resolution of only 2 % for energies above 500 keV, which is better than in large-scale experiments [12],[38]. Without the coating, the detector geometry suggests a light collection efficiency of around 20 %,

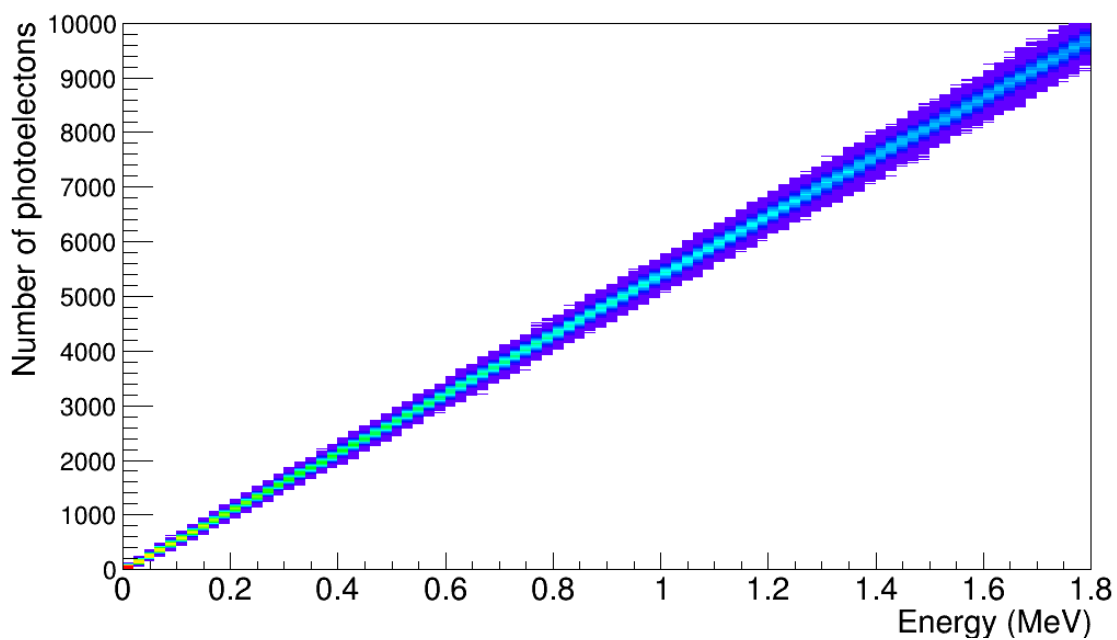
comparing to 53 % with the coating. This is likely unrealistic for this detector setup and thus motivating the running of the simulations also without the foil. The VM2000 implementation in Geant4 has been studied and verified [37] previously, which leads to believe that the unrealistic detector efficiency stems from the ideal conditions in the simulation. For example, the interface between the coating and the detector is perfect with no air pockets or creases between or in the materials. VM2000 is assumed to have a reflectance of 99 % [37], meaning that in average, one collision in a hundred results in absorption of the photon. In reality, though the theoretical reflectivity of VM2000 could be 99 %, photons are also lost in the imperfect reflections. All things considered, the light collection efficiency in the actual experiment is expected to be somewhere between the two simulated cases.

In Fig. 15, the effect of reflections to the energy resolution spectrum is depicted. If all reflections from the container surface are removed (red) or if teflon coating is used around the inner surface of the container edges (black), the resulting spectrum takes approximately a Gaussian form. In addition, this is also observed with the VM2000 coating where a Gaussian peak is formed but with approximately double the number of photoelectrons than in other cases. However, allowing natural reflections from container surface, a distribution resembling a combination of two different Gaussian distributions is observed (green). As is seen in Fig. 17a, the curve is in fact a combination of multiple Gaussian distributions related to the initial location of the event. Interestingly, adding teflon coating doesn't increase light collection (mean = 392 number of photoelectrons) compared to without coating (mean = 409 number of photoelectrons). This implies that all photons that reach the PMTs are reflected in such a low angles from the container that are within total internal reflection angle range of quartz-air interface.

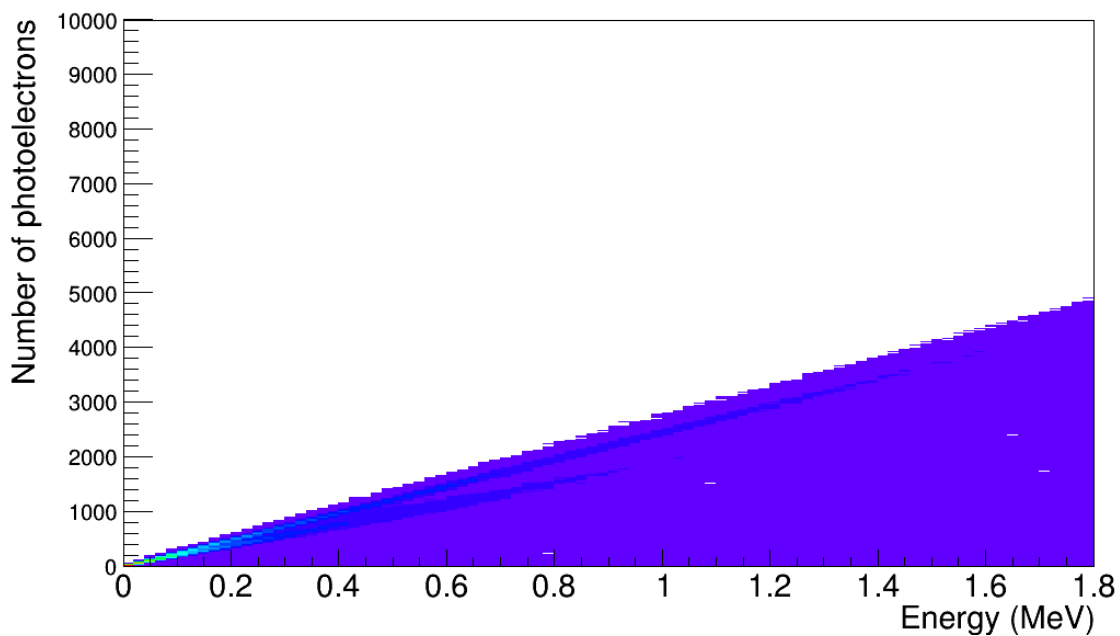
The effect of container surface treatment to light collection is highlighted in Fig. 16, which shows simple two dimensional approximations of the setup with four different container surface options discussed above. The first picture in Fig. 16 represents a case with the Teflon coating, the second is without any coatings, the third is not allowing reflections inside the container and finally at the bottom is the fully coated setup. As we can see from the pictures, only coating the container does not seem to increase rays hitting the end plates representing the PMTs when compared to no coating. Not surprisingly, not allowing reflections inside the container does reduce the light output, whereas coating the setup with ideal reflector ultimately collects all rays to the end points, assuming no loss of photons. Interestingly, when the setup is fully coated, it clearly takes a long distance for some rays to reach the PMTs, judging from the massive amount of ray paths shown in the picture.

The Gaussian peaks emerging from the detector geometry is closely related to the radial distance of the event from the cylinder axis of the container as seen in Fig. 17a. The geometry of the setup favors events near the edges of the liquid where the more photons are able to reach the PMTs. However, the presence of the coating around the container and the light guides negates this effect, thus the coating is vital in obtaining good energy resolution. As the actual coating is not as perfect as in the simulation, some position dependency of the energy response is expected in the actual experiment.

Even though the detector performance is best near the edges of the containers, events very close to the edge lead to poor light yield. In Fig. 17b, the number of photoelectrons

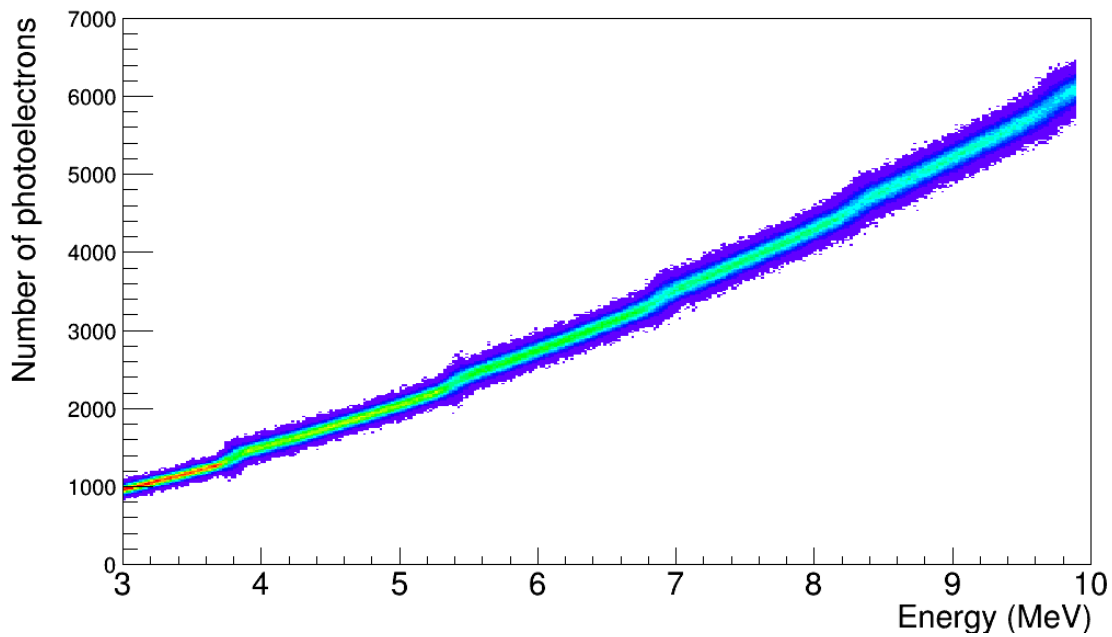


(a) Number of collected photoelectrons as a function of electron energy with the VM2000 coating.

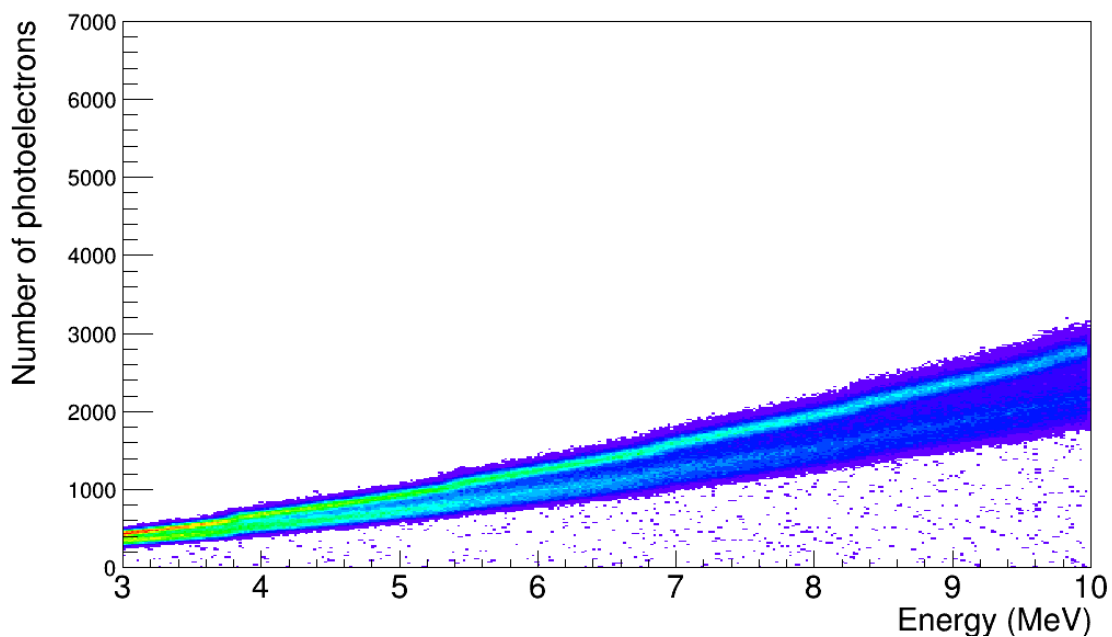


(b) Number of collected photoelectrons as a function of electron energy without coating.

Figure 13: Number of collected photoelectrons as a function of electron energy. With coating, more photons are counted resulting in greater accuracy. Brighter color indicates higher density.



(a) Number of collected photoelectrons as a function of alpha particle energy with the VM2000 coating.



(b) Number of collected photoelectrons as a function of alpha particle energy without coating

Figure 14: Number of collected photoelectrons as a function of alpha particle energy. As with electrons, more photons are counted with greater accuracy if VM2000 is used. The bumps in the curves are artefacts of the simulation engine but have no significant impact to the results. In addition, realistic sequencing for alpha particles is assumed in the simulations.

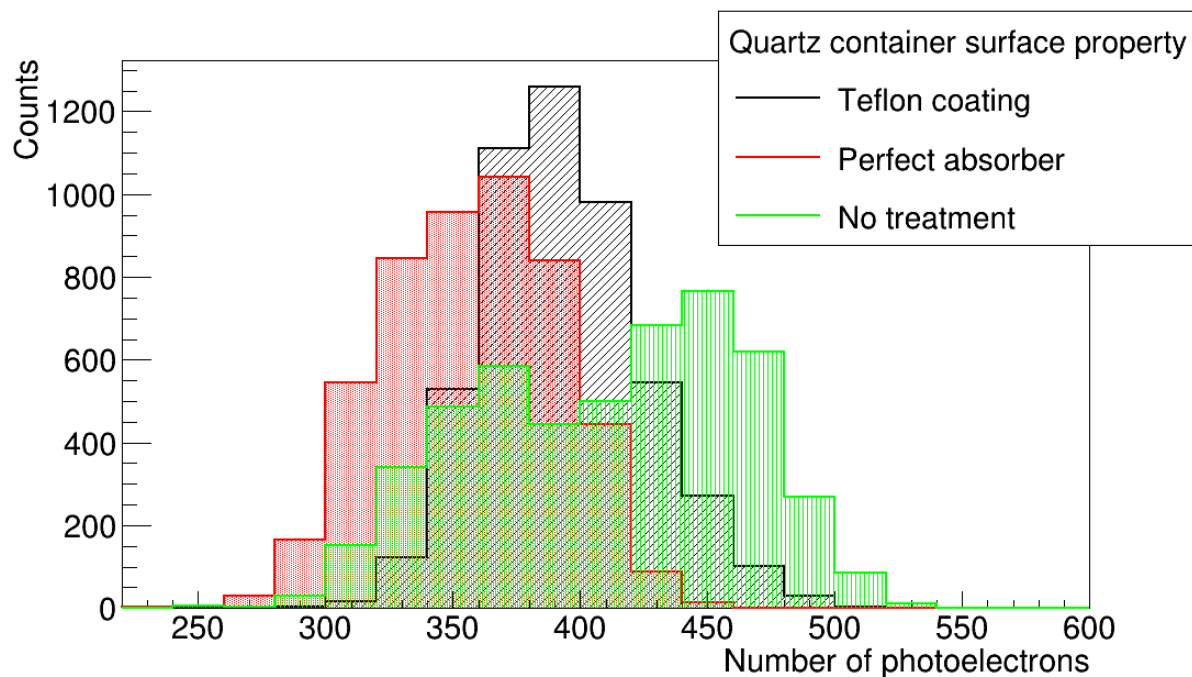


Figure 15: Light production of 0.2 MeV electrons in LAB with three different container surface options. In the perfect absorber case, all photons hitting the container surface are terminated. No treatment option refers to a quartz - LAB interface at the container boundary.

as a function of distance from the cylinder axis is presented. It is seen how the number of photoelectrons increase as the radius increases, but drop very close to the edge. Change in the color reflects the fact that more events occur in the edges than in the center region due to the cylindrical geometry.

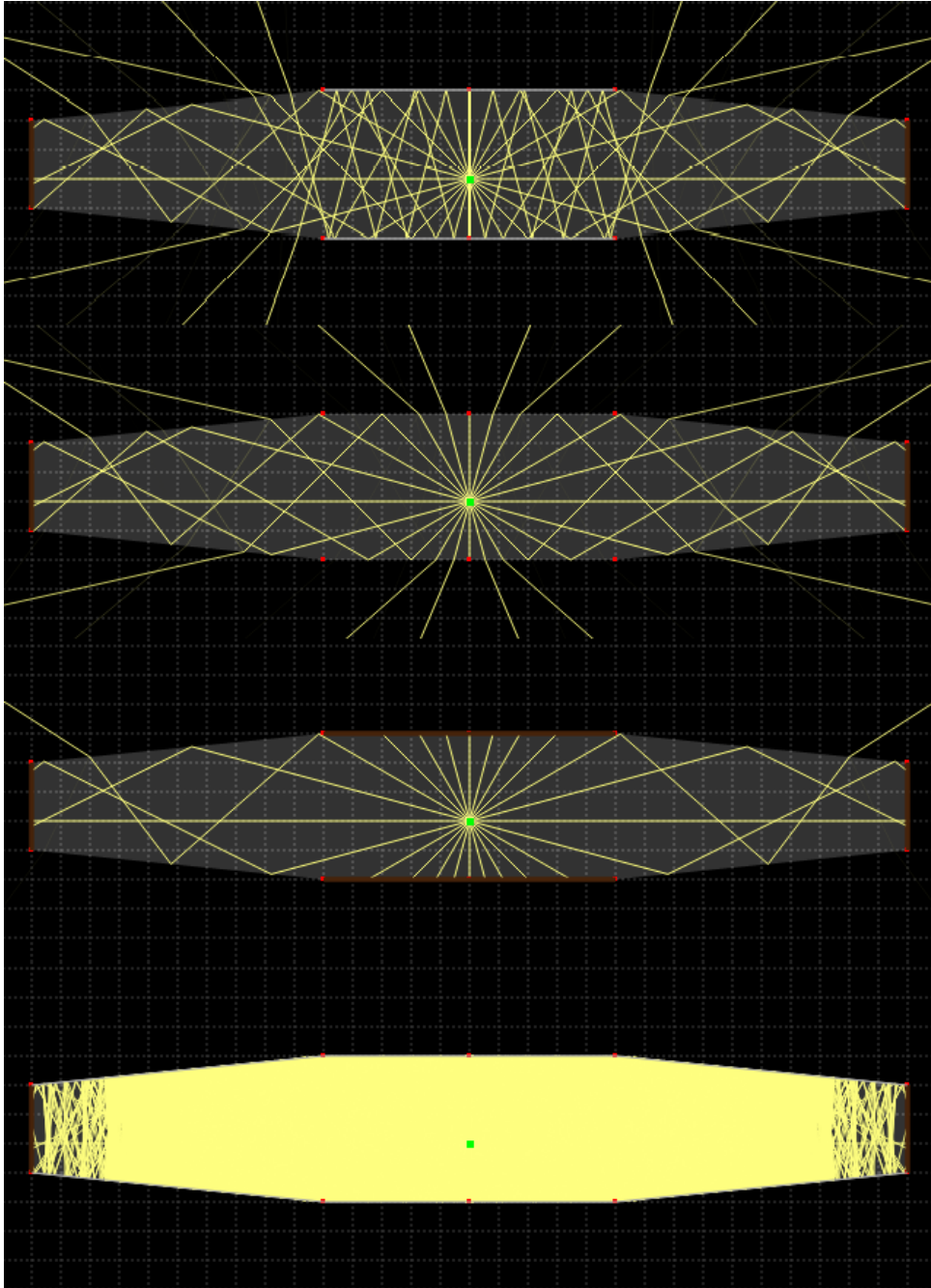
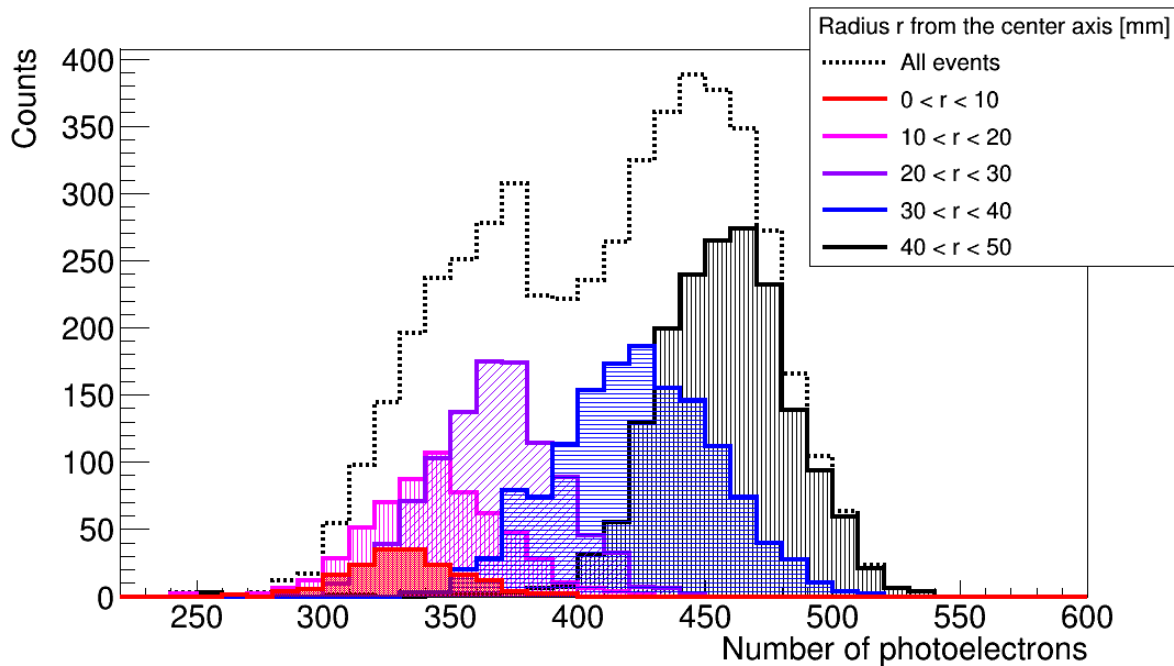
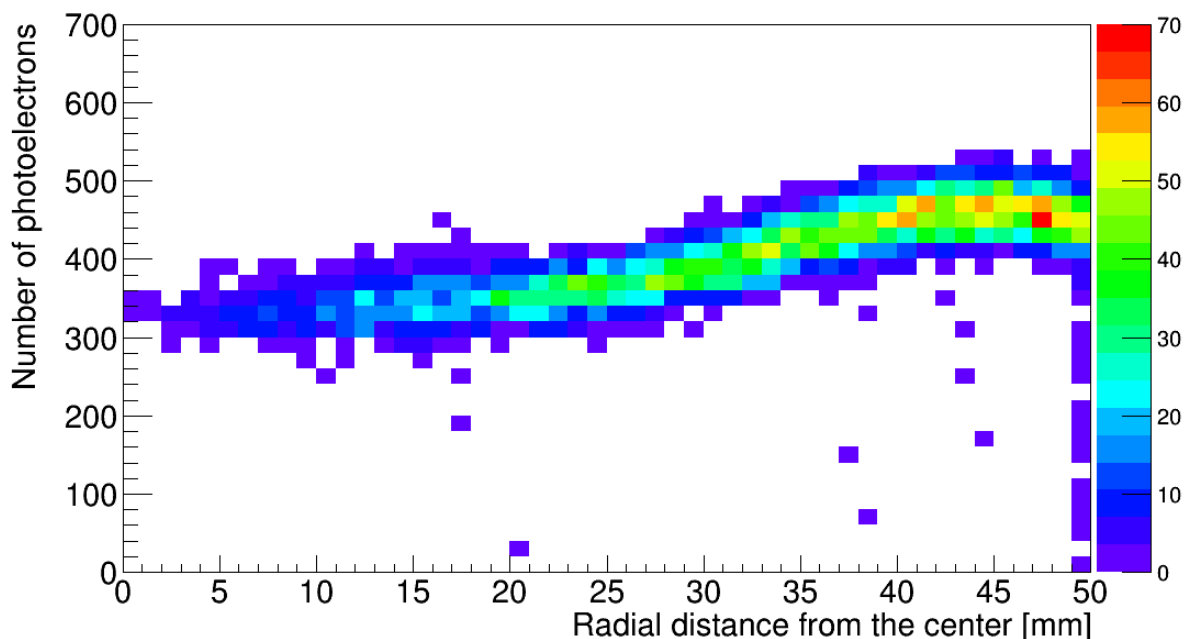


Figure 16: Schematic 2D presentations of photon reflections in different surface treatments in this detector geometry. Pictures from top: (1) Ideal coating inside container, (2) No coating, (3) No reflections from container, (4) Ideal coating in both the container and the light guides.



(a) Number of photoelectrons as a function of radial distance from the longitudinal axis of the container without reflective foil. Events near the edges of the container generally produce more light and more uniform distribution.



(b) Number of photoelectrons as a function of distance from the longitudinal axis. Near the edge of the container the number of photoelectrons drop due to most of the photons escaping the detector.

Figure 17: The number of photoelectrons observed as a function of the radial distance of the event. Events near the edges of the container yield more photons. Here 5000 electrons with energy of 0.2 MeV were simulated without any coating.

## 5.2 Background spectra

In the C14 experiment, the intrinsic background comes from four different sources: radioactivity inside the liquid, gamma rays from light guides, container and the PMTs. However, contribution from the light guides and the container is negligible as the activities of the radioactive contaminants equals roughly 150 (container) to 1500 (light guides) times lower than in the PMT (Tab. 3). The gamma ray intensity from the PMTs falls to 19.5 % in the 20 cm distance and to 3.8 % in the 40 cm distance (see Fig. 22) from absorption of the light guides, yet the intensity even then is tenfold compared to liquid's gamma ray intensity. As a result, the gamma rays from sources other than the PMTs can be safely excluded in the simulations.

The measurement time window was set to be 28 days, leading to 5514  $^{14}\text{C}$  decays in a 1.6 liter liquid, assuming radiocarbon concentration  $10^{-17}$ , a value that is fairly typical in organic scintillators [39]. The exact concentrations of background components were not known, so a number of realistic scenarios for concentrations were analyzed. From the beginning it was clear that the radioimpurity concentrations of the purified liquid would cause negligible background, and so for uranium, thorium and potassium a relatively high concentration was considered. As with the energy resolution study, many of the background simulations were run both with and without the VM2000 coating.

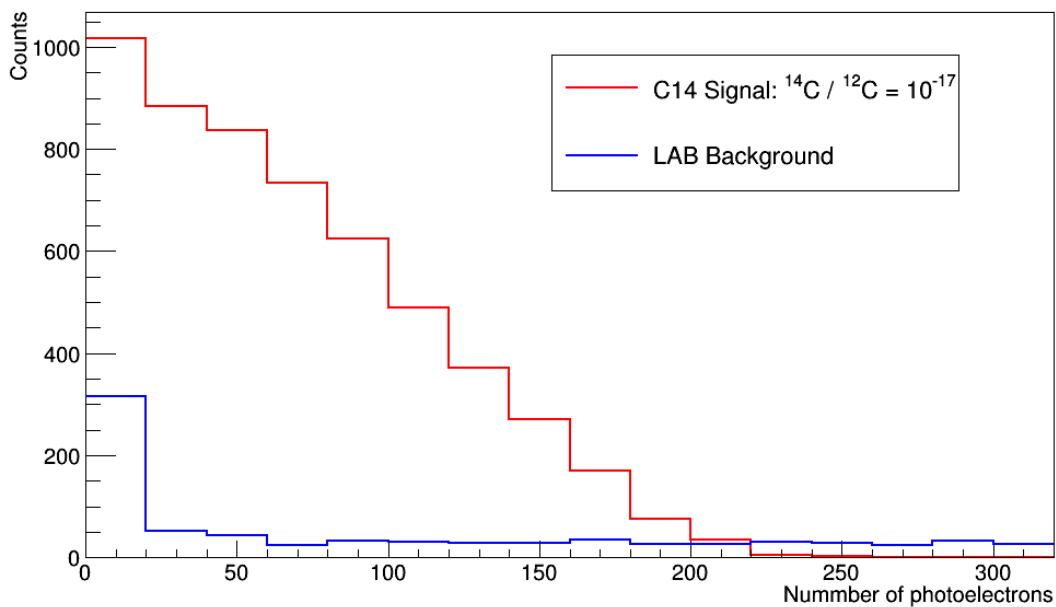
### 5.2.1 LAB background spectrum

Here the energy resolution data was employed to create the simulated background spectra. First, the "pure" (not affected by the detector setup) decay spectra for all contaminants were created by simulating a sample of five million radioactive decays per isotope and recording the number of electrons, alpha particles and positrons emitted along with their energies. A Fig. 12 shows an example of  $\beta$  (electron) spectrum for  $^{14}\text{C}$ . Next the obtained pure spectra were sampled with the energy resolution data and the  $(28 \pm 2)$  % quantum efficiency to get the actual simulated background spectrum for each component. Last, the aggregate background spectrum was created as a sum of all the individual components.

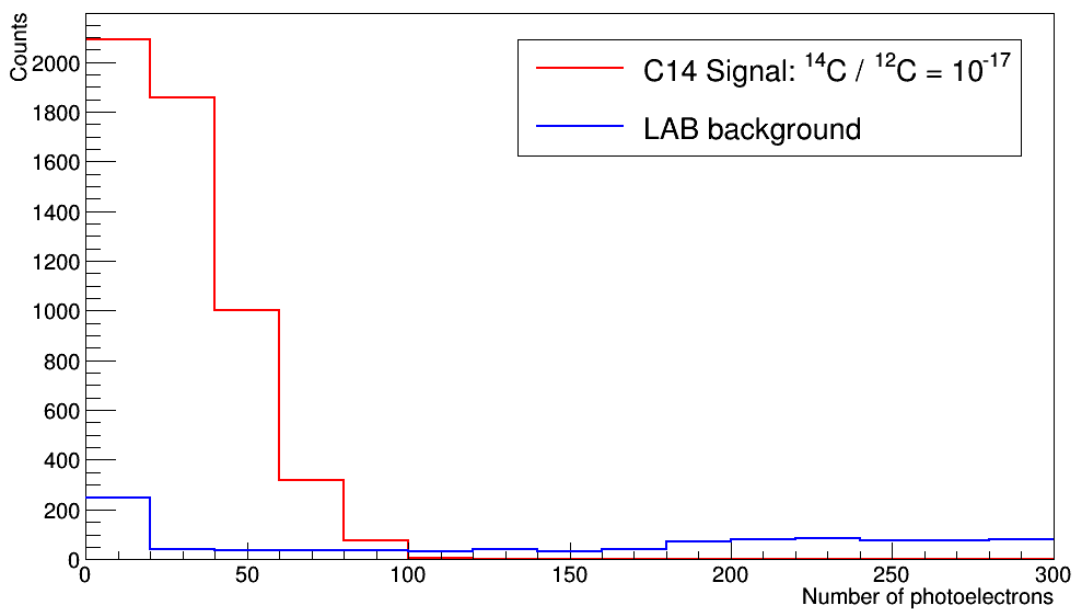
In a large scale liquid scintillator experiment, the liquid would be one of the largest background sources and is typically very rigorously purified (see for example [22]). This is especially needed when the scintillator mass is of the order of kilotons. However, using these purified contaminant values would correspond to a nBq scale activities for the three common isotopes  $^{238}\text{U}$ ,  $^{232}\text{Th}$  and  $^{40}\text{K}$  in a 1.6 liter volume (Tab. 3). In other words, one would expect a decay once in a few decades. For this reason a higher concentration, approximately 10000 times the purified values, were used for uranium, thorium and potassium inside the liquid. This is likely more than is observed even without the purification, but it highlights the shape of the background spectrum. A secular equilibrium is assumed for isotopes in the uranium and thorium decay chains. An exception to this is caused by  $^{222}\text{Rn}$  in the uranium chain, which concentration is also affected by contamination from air. Therefore, the concentration of isotopes below  $^{222}\text{Rn}$  in the decay chain is assumed to have concentrations that of radon's.

The background spectra of LAB is presented in Fig. 18. The concentrations used were  $^{14}\text{C} = 10^{-17}$  g/g,  $^{238}\text{U} = ^{232}\text{Th} = ^{40}\text{K} = 0.123$  mBq,  $^{85}\text{Kr} = 0.070$  mBq and  $^{222}\text{Rn} = 1.57$   $\mu\text{Bq}$ . The figures show that the background spectrum has little effect compared to the

$^{14}\text{C}$  signal, regardless of the coating. Increasing the radon concentration by a factor of 1000 increases background but not by a significant amount compared to the  $^{14}\text{C}$  signal. In Fig. 19 the LAB background using two different  $^{222}\text{Rn}$  concentrations of  $1\text{ mBq/m}^3$  and  $1\text{ Bq/m}^3$  is presented. Most notably, large radon concentration leads to a bump in the background spectrum but this bump is located far beyond the endpoint of  $^{14}\text{C}$  signal at around 400 keV and thus has no impact on the measurement.

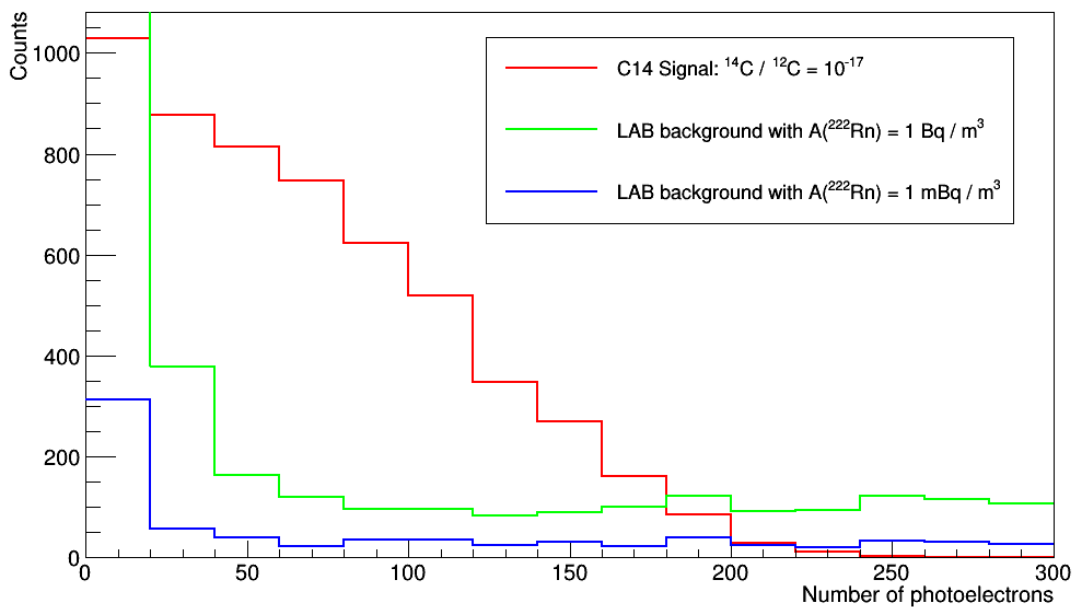


(a) LAB background with the VM2000 coating.

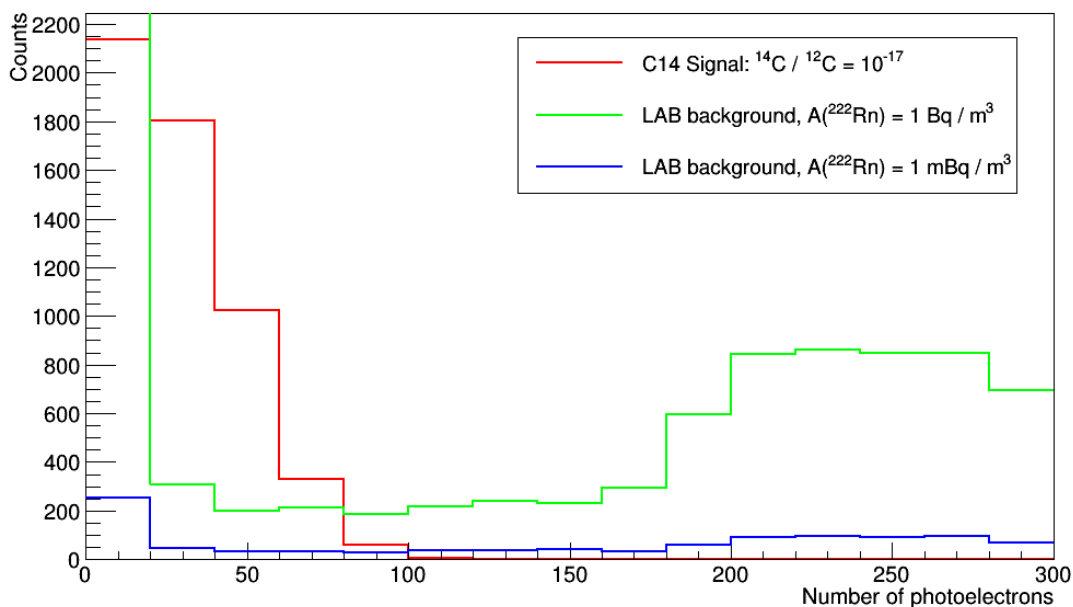


(b) LAB background without coating.

Figure 18: LAB background compared to the  $^{14}\text{C}$ . In both cases, the background level is negligible.



(a) LAB background with the VM2000 coating.



(b) LAB background without coating.

Figure 19: LAB background with  $A(^{222}\text{Rn}) = 1 \text{ mBq/m}^3$  and  $1 \text{ Bq/m}^3$ . Even with the larger radon concentration, the LAB background remains small compared to the  $^{14}\text{C}$  signal.

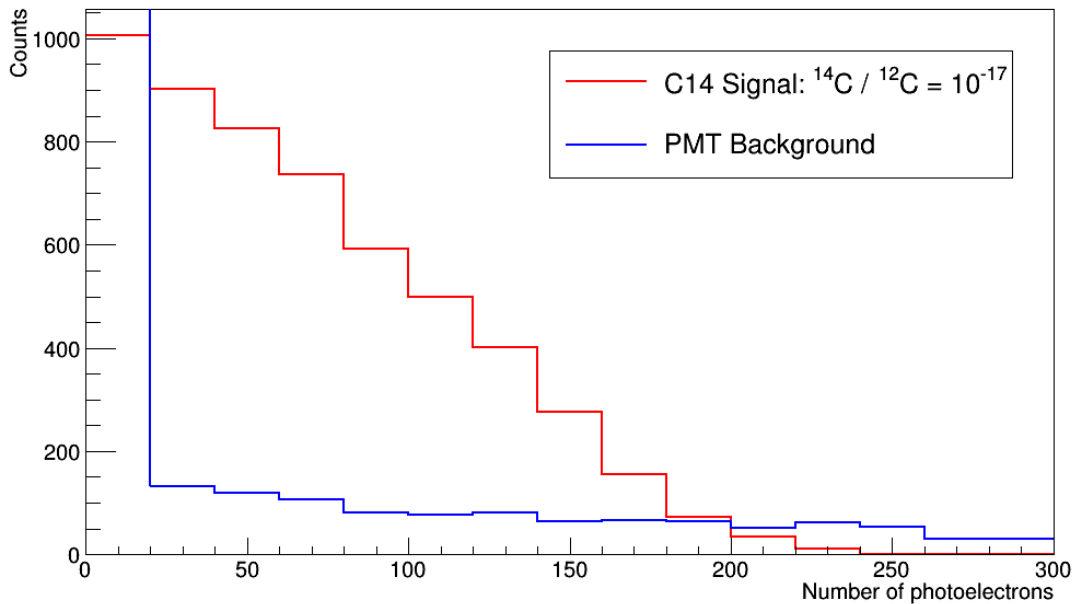
### 5.2.2 PMT background spectrum

The algorithm for measuring PMT background was straightforward. First, the radioactive isotopes were simulated to decay in the PMT surface and their gamma energy spectra were recorded. Next, a number of gamma rays were beamed towards the scintillator corresponding to the expected activity of the isotope in question. The energies of the gamma rays were sampled from the simulated energy distributions.

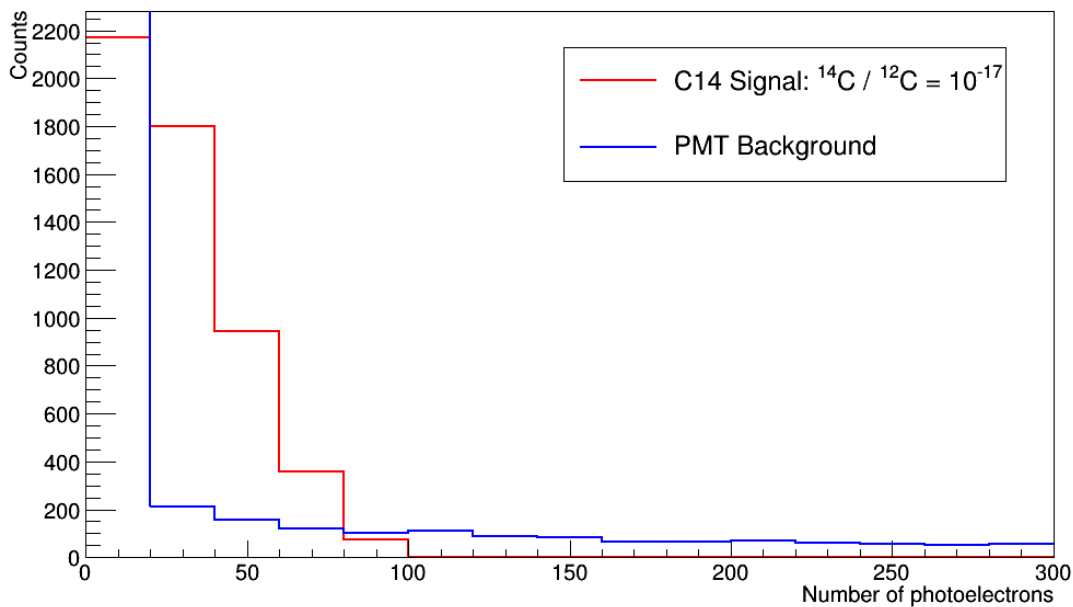
Comparing to LAB background spectrum, the background from PMTs is much greater, though the impact to the signal is still small. In figures 20a and 20b the distance from the PMTs to the sample is 20 cm which theoretically equals to approximately 80 % loss in gamma ray intensity. The values of radionuclide activities are as in Tab. 3. However, in a another source [40], activities of  $^{238}\text{U} = 220$  mBq,  $^{232}\text{Th} = 24$  mBq and  $^{40}\text{K} = 420$  mBq were given. These values are several times larger than those used before. Therefore, a comparison between these two set of values is presented in Fig. 21. The difference in the background level is noticeable. Now the background from the PMTs is greater than C14 signal for values above 150 photoelectrons. As a result, if the measured PMT gamma levels are close to the larger values, it might be necessary to move the PMTs further away from the sample. As expected, moving the PMTs twice as far reduces background from them significantly. Theoretically, only around 4 % of gamma rays penetrate to the sample due to increase in distance. This is highlighted in Fig. 22.

### 5.2.3 Comparison with lower $^{14}\text{C}$ concentration

Figures 23a and 23b show the  $^{14}\text{C}$  signal compared to the full background spectrum (LAB + PMTs) with two different concentrations of  $^{14}\text{C}$  when measured for 28 days. Activities of background components are as in Tab. 3. In the experiment it is desired to find a sample with  $^{14}\text{C}$  concentration even lower than  $10^{-18}$  so at least with these background concentrations the C14 signal would be weaker than the background. This is not necessarily a concern when the background spectrum is well known and could be subtracted from the results.



(a) PMT background with the VM2000 coating.



(b) PMT background without coating.

Figure 20: PMT background and the  $^{14}\text{C}$  signal. The background is larger than LAB background but still low compared to the signal.

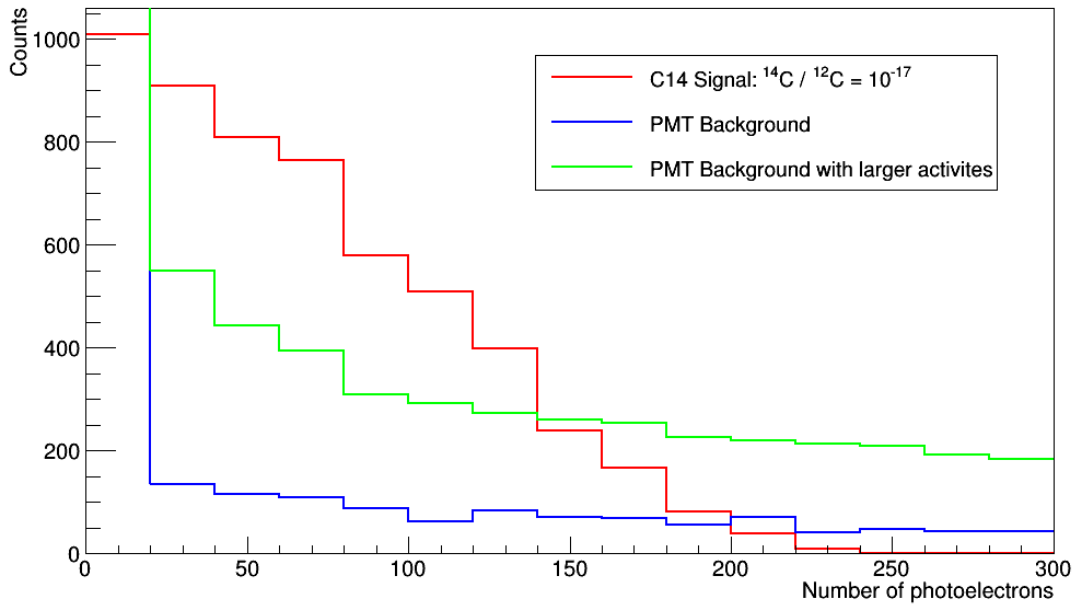


Figure 21: PMT background with two different radiocontaminant activities. The larger activities are  $^{238}\text{U} = 220$  mBq,  $^{232}\text{Th} = 24$  mBq and  $^{40}\text{K} = 420$  mBq whereas the lower are 82 mBq, 44 mBq, 27 mBq for U, Th and K, respectively.

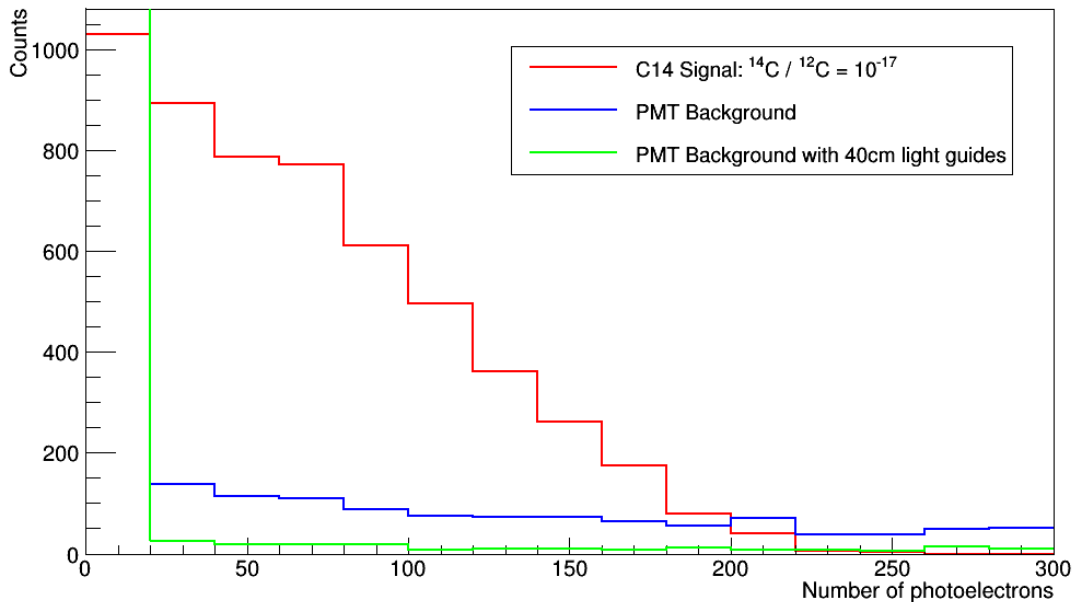
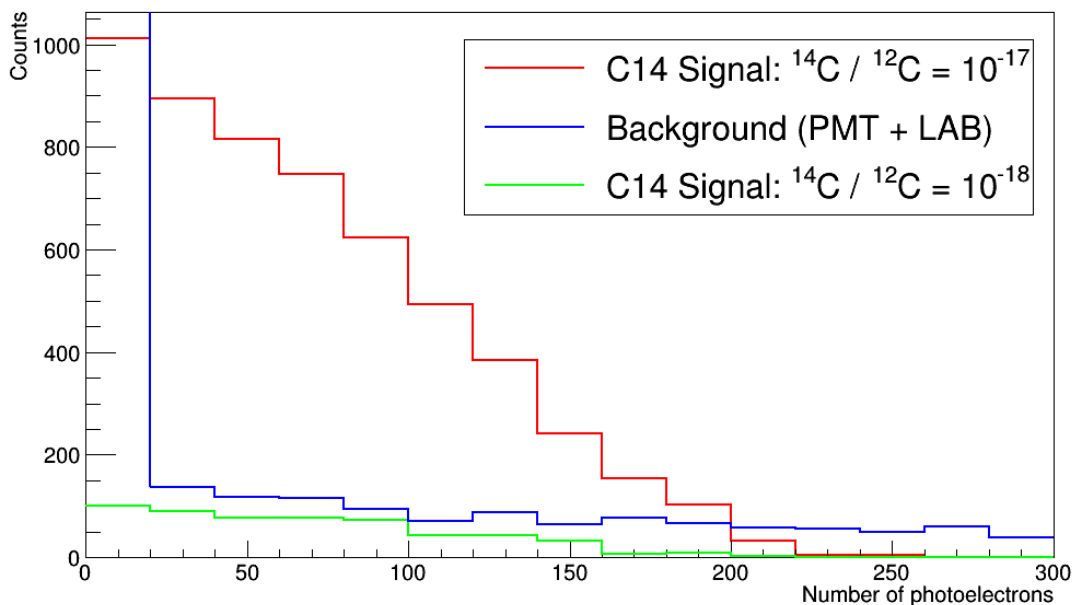
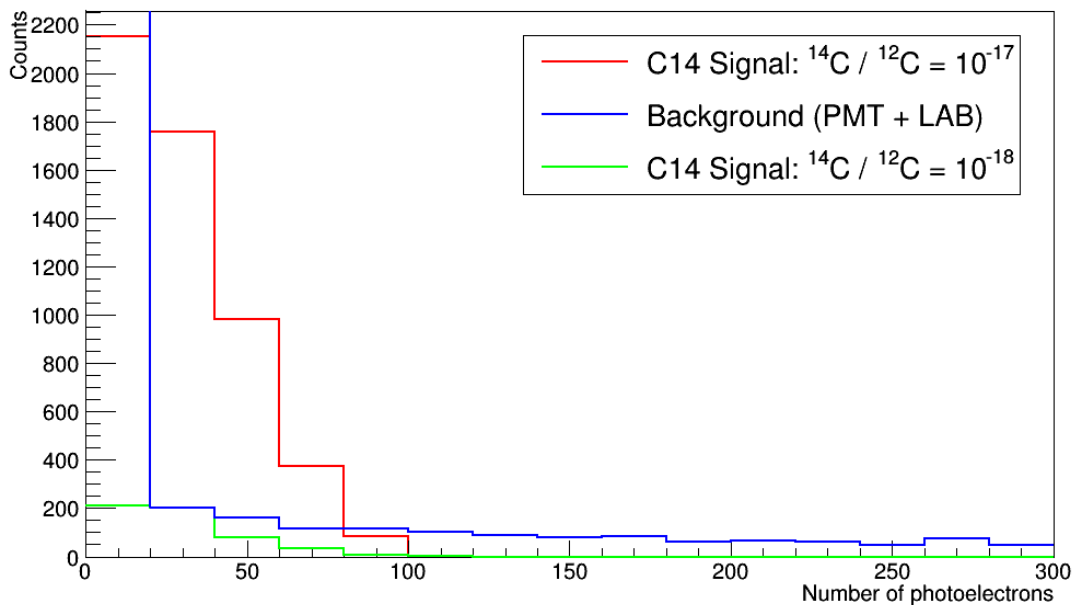


Figure 22: PMT background with two different light guide lengths using the smaller background activities. As expected, the background level drops significantly as the distance from the PMTs to the bulk is doubled.



(a) Complete intrinsic background with the VM2000 implementation.



(b) Complete intrinsic background without coating.

Figure 23: Intrinsic background and the  $^{14}\text{C}$  signal with two different concentrations of  $^{14}\text{C}$ . With ten times less  $^{14}\text{C}$ , the background is larger than the signal by a fair amount.

## 6 SUMMARY & OUTLOOK

In this study a simulation environment utilizing Geant4 simulation toolkit was constructed to the study of an upcoming C14 experiment in the Pyhäsalmi Mine, Finland. The simulation environment was used to study the detector energy response with and without reflective coating for electrons and alpha particles. The results were used to simulate intrinsic background spectra of LAB scintillator liquid and photomultiplier tubes and compared against simulated  $^{14}\text{C}$  signal.

It was found that the detector energy response is heavily position dependent if no reflective foil is used to cover the detector. The response is a sum of multiple Gaussian peaks each characteristic to the radial distance of the event origin from cylinder axis of the detector. The events generated near the edges of the container yield more light than events near the center. Using the reflective coating negates this effect completely and as such improves the energy response. Accounting for the quantum efficiency (28 %) of the PMTs, a detector efficiency of 7-15 % is expected, depending on the real reflectance of the coating.

The main contributor to the intrinsic background signal is coming from the photomultiplier tubes. Since the volume of the LAB sample is small, even contaminant activities thousands of times larger than in previous large scale experiments do not contribute much to the background signal. Moreover, the gamma radiation from the acrylic light guides and quartz glass container can be neglected. A  $1 \text{ Bq/m}^3$  concentration of  $^{222}\text{Rn}$  in the sample does increase LAB background to a level where it could distract the measurement, therefore the sample should be protected from radon contamination as much as possible. Finally, depending on the measured activities of the tubes, it might be necessary to move the tubes further away from the sample in order to reduce gamma radiation to the sample.

This study could be expanded to include external background sources, for example muons and gamma radiation from surrounding materials. It would require some additions to the current simulation environment, as now it does not include lead and copper shielding and rock overburden, for example. Currently, the simulation could be used to study other scintillator materials besides LAB. Most importantly, a method for adjusting the detector energy response should be added in order to calibrate the simulation environment to match the actual measurements. This could be done by adjusting coating reflectance parameter in the simulation, for example.

## REFERENCES

- [1] BOREXINO COLLABORATION *Science and technology of Borexino: a real-time detector for low energy solar neutrinos* *Astroparticle Physics* 16, 205-234, 2002
- [2] S. FUKUDA ET AL. *The Super-Kamiokande detector* *Nuclear Instruments and Methods in Physics Research A* 501 (2-3): 418-462
- [3] CURRENT STATUS AND FUTURE PROSPECTS OF THE SNO+ EXPERIMENT *SNO+ Collaboration Advances in High Energy Physics*, vol. 2016, 6194250
- [4] F. FERRER, L. M. KRAUSS, S. PROFUMO *Indirect detection of light neutralino dark matter in the NMSSM* *Phys.Rev.D*74:115007, 2006
- [5] SARAH QUIRK *Purification of liquid scintillator and Monte Carlo simulations of relevant internal backgrounds in SNO+* Master's thesis, Queen's university, 2008
- [6] G. HEUSSER *Low-radioactivity background techniques* *Annu. Rev. Nucl. Part. Sci.* 1995. 45:543-90
- [7] MICHAEL WURM *Cosmic background discrimination for the rare neutrino event search in Borexino and Lena* Technische Universität München
- [8] G. A. KOVALTSOV, A. MISHEV, I. G. USOSKIN *A new model of cosmogenic production of radiocarbon  $^{14}\text{C}$  in the atmosphere* *Earth Planet. Sci. Lett.*, 337, 114-120, 2012
- [9] THE BOREXINO COLLABORATION *Final results of Borexino Phase-I on low energy solar neutrino spectroscopy* *Phys. Rev. D* 89, 112007 (2014)
- [10] JU.M. GAVRILJUK ET AL. *Working characteristics of the New Low-Background Laboratory (DULB-4900)* *Nucl. Instrum. Methods A* 729 (2013) 576
- [11] THE BOREXINO COLLABORATION *Measurement of the  $^{14}\text{C}$  abundance in a low-background liquid scintillator* *Phys. Lett. B* 422 (1998) 349
- [12] JUNO COLLABORATION *Neutrino Physics with JUNO* *J. Phys. G* 43 (2016) 030401
- [13] RANDALL D. KNIGHT *Physics for scientists and engineers* Pearson 2008
- [14] J. KENNETH SHULTIS: *Fundamentals of Nuclear Science and Engineering*. Marcel Dekker, 2002
- [15] JARI JOUTSENVAAARA *Deeper understanding at Lab 2: the new experimental hall at Callio Lab underground centre for science and R & D in the Pyhäsalmi Mine, Finland* Master's thesis, Oulu University, 2016
- [16] BOREXINO COLLABORATION *Measurements of extremely low radioactivity levels in BOREXINO* *Astropart.Phys.*18:1-25, 2002
- [17] TIMO ENQVIST ET AL. *Measurements of muon flux in the Pyhäsalmi underground laboratory* *Nucl.Instrum.Meth.* A554 (2005) 286-290

- [18] J.N. ABDURASHITOV ET AL. *Measurement of neutron background at the Pyhäsalmi mine for CUPP project, Finland* arXiv:nucl-ex/0607024
- [19] G. HEUSSER *Low-Radioactivity Background Techniques* Annu. Rev. Nucl. Part. Sci. 1995. 45.543-90
- [20] BOREXINO COLLABORATION *Precision Measurement of the  $^7\text{Be}$  Solar Neutrino Interaction Rate in Borexino* PRL 107, 141302 (2011)
- [21] JUNO COLLABORATION *Simulation of natural radioactivity backgrounds in the JUNO central detector* arXiv:1505.03215v1
- [22] BENZIGER, J.B. ET AL. *Borexino: A Scintillator Purification System for a Large Scale Solar Neutrino Experiment* Nucl.Instrum.Meth. A417 (1998) 278-296
- [23] GLENN F. KNOLL *Radiation detection and measurement, third edition* John Wiley & Sons Inc., 2000
- [24] WILLIAM R. LEO *Techniques for nuclear and particle physics experiments* Springer-Verlag, 1987
- [25] J. B. BIRKS: *The Theory and Practice of Scintillation Counting* Elsevier, 1964
- [26] BOREXINO COLLABORATION *Pulse-Shape discrimination with the Counting Test Facility* Nucl.Instrum.Meth.A584:98-113, 2008
- [27] DONALD L. HORROCKS *Applications of liquid scintillation counting* Academic Press, 1974
- [28] C. BUCK ET. AL. *Measuring the  $^{14}\text{C}$  isotope concentration in a liquid organic scintillator at a small-volume setup* Instruments and Experimental Techniques 55(1), 2012
- [29] TIMO ENQVIST ET AL. *Towards  $^{14}\text{C}$ -free liquid scintillator*, *Journal of Physics: Conference Series*. To be published (Proceedings of Neutrino2016, London)
- [30] MICHAEL WURM *The next-generation liquid-scintillator neutrino observatory LENA* arXiv:1104.5620
- [31] *Pubchem database* [https://pubchem.ncbi.nlm.nih.gov/compound/2\\_5-Diphenyloxazole#section=Top](https://pubchem.ncbi.nlm.nih.gov/compound/2_5-Diphenyloxazole#section=Top), accessed 21.08.2016
- [32] ET ENTERPRISES *ET 9302B series data sheet* <https://my.et-enterprises.com/pdf/9302B.pdf>, accessed 21.08.2016
- [33] *Geant4 simulation toolkit* <https://geant4.web.cern.ch/geant4/>
- [34] *ENSDF database* [www.nndc.bnl.gov/ensdf](http://www.nndc.bnl.gov/ensdf)
- [35] STEFFEN HAUF ET AL. *Radioactive decays in Geant4* arXiv:1307.0996
- [36] D. E. CULLEN *A simple model of photon transport* Nuclear Instruments and Methods in Physics Research B 101 (1995) 499-510
- [37] MARTIN JANECEK AND WILLIAM W. MOSES *Simulating Scintillator Light Collection Using Measured Optical Reflectance* IEEE Transactions On Nuclear Science, Vol. 57, No. 3, June 2010

- [38] KAMLAND RCNS GROUP *An Overview of the KamLAND 1-kiloton Liquid Scintillator* arXiv:physics/0404071v2
- [39] G. BONVICINI ET AL. THE CHEMICAL HISTORY OF  $^{14}\text{C}$  IN DEEP OILFIELDS hep-ex/0308025v2 (8 Aug 2003)
- [40] J. AMARE ET AL. *ANAIS status report* Journal of Physics: Conference Series 203 (2010) 012044
- [41] RENE BRUN AND FONS RADEMAKERS *ROOT: An object oriented data analysis framework* Nuclear Instruments and Methods in Physics Research Section A: Accelerators, Spectrometers, Detectors and Associated Equipment, Volume 389, Issues 1-2, 11 April 1997, Pages 81-86